Journal of Magnetic Resonance 308 (2019) 106560

Contents lists available at ScienceDirect

Journal of Magnetic Resonance

journal homepage: www.elsevier.com/locate/jmr

UWB DEER and RIDME distance measurements in Cu(II)–Cu(II) spin pairs

Frauke D. Breitgoff[a,*,1], Katharina Keller[a,*,1], Mian Qi[b], Daniel Klose[a], Maxim Yulikov[a], Adelheid Godt[b,*], Gunnar Jeschke[a]

[a] ETH Zürich, Lab. Phys. Chem., Vladimir-Prelog-Weg 2, 8063 Zürich 3 Switzerland
[b] Faculty of Chemistry and Center for Molecular Materials (CM_2), Bielefeld University, Universitätsstraße 25, 33615 Bielefeld, Germany

ARTICLE INFO

Article history:
Received 7 June 2019
Revised 12 July 2019
Accepted 15 July 2019
Available online 18 July 2019

Keywords:
EPR
Cu(II)
RIDME
DEER
PELDOR
Broadband excitation
Adiabatic pulses
Dipolar spectroscopy
Ultra-wideband (UWB)

ABSTRACT

Distance determination by Electron Paramagnetic Resonance (EPR) based on measurements of the dipolar coupling are technically challenging for electron spin systems with broad spectra due to comparatively narrow microwave pulse excitation bandwidths. With $Na_4[\{Cu^{II}(PyMTA)\}$-(stiff spacer)-$\{Cu^{II}(PyMTA)\}]$ as a model compound, we compared DEER and RIDME measurements and investigated the use of frequency-swept pulses. We found very large improvements in sensitivity when substituting the monochromatic pump pulse by a frequency-swept one in DEER experiments with monochromatic observer pulses. This effect was especially strong in X band, where nearly the whole spectrum can be included in the experiment. The RIDME experiment is characterised by a trade-off in signal intensity and modulation depth. Optimal parameters are further influenced by varying steepness of the background decay. A simple 2-point optimization experiment was found to serve as good estimate to identify the mixing time of highest sensitivity. Using frequency-swept pulses in the observer sequences resulted in lower SNR in both the RIDME and the DEER experiment. Orientation selectivity was found to vary in both experiments with the detection position as well as with the settings of the pump pulse in DEER. In RIDME, orientation selection by relaxation anisotropy of the inverted spin appeared to be negligible as form factors remain relatively constant with varying mixing time. This reduces the overall observed orientation selection to the one given by the detection position. Field-averaged data from RIDME and DEER with a shaped pump pulse resulted in the same dipolar spectrum. We found that both methods have their advantages and disadvantages for given instrumental limitations and sample properties. Thus the choice of method depends on the situation at hand and we discuss which parameters should be considered for optimization.

1. Introduction

Knowledge of the structure of biological macromolecules is often crucial for understanding their function [1,2]. However, structural information is often difficult to attain for such complex systems and modelling usually relies on combining information obtained by different techniques [3,4]. A variety of methods has been developed: Crystallizable parts of protein complexes can be characterized by X-ray crystallography [5] and NMR techniques can yield short-range distance restraints for structure determination [6,7]. Mass spectrometry (MS) can be used in combination with resolving ion size (ion mobility) [8,9], dissociation properties (tandem mass spectrometry) [10] or reactivity (for example H/D exchange) [11] or as native MS [12]. Further methods include fluorescence spectroscopy, specifically Förster Resonance Energy Transfer (FRET) [13,14], and *cryo*-Electron Microscopy [15,16]. Among these fields, Pulsed Dipolar Spectroscopy (PDS) by Electron Paramagnetic Resonance (EPR) represents a unique method as it can provide long-range distance distributions for systems with and without long-range order with an upper limit of 4–6 nm [17–19] to 16 nm [20], depending on the spin environment. Distance distribution information by PDS can provide a snapshot of the conformational ensemble or be used to solve structures [21], e.g. by hybrid structural modeling [22,23].

PDS experiments determine the distance distribution between two spin centers in the sample. Often, these centers are engineered by site-directed spin labeling [24–27] of the macromolecule. Naturally occurring metal centers, however, are also abundant [1,28–30]. Such systems include metallo-enzymes pivotal to many processes of life such as haemoglobin [31]. If the metal center in its natural oxidation state and ligand field does not possess a spin, i.e. one or more unpaired electrons, it can often be substituted by a

* Corresponding authors.
E-mail addresses: frauke.breitgoff@phys.chem.ethz.ch (F.D. Breitgoff), katharina.keller@phys.chem.ethz.ch (K. Keller), godt@uni-bielefeld.de (A. Godt).
[1] These authors contributed equally.

https://doi.org/10.1016/j.jmr.2019.07.047
1090-7807/

paramagnetic ion to allow for EPR and paramagnetic NMR measurements [32–35].

Furthermore, spin labels containing metal centers are the subject of ongoing method development [36–40]. Due to their chemical inertness, redox stability and non-toxicity [3] they are promising candidates for *in-cell* experiments. *In-cell* Gd-Gd distance measurements have been demonstrated [41–45] and show promise for longer spin-label lifetimes than possible in *in-cell* measurements between commonly used types of nitroxides [46,47]. Nitroxides that are more reduction resistant than the commonly used nitroxides are being developed [48]. In addition, metal-based spin labels represent building blocks for the development of orthogonal labeling schemes which can be combined with spectroscopic selection in pulse EPR experiments [49–51].

EPR spectra – especially of metal ions but also from other spin centers – often span several GHz [28]. Broadening can be orientation dependent or can stem from distributions of particular spectroscopic parameters. Important examples are anisotropic electron Zeeman and hyperfine interactions, characterized by the g-tensor or hyperfine tensor anisotropies, as well as in high-spin systems the joint effect of g-tensor and zero-field splitting interaction caused by strong electron-electron interactions. The maximal achievable excitation bandwidth by monochromatic pulses in EPR is, with about one hundred MHz, rather narrow. Sensitive measurements of systems with broad spectra are therefore challenging and more prone to effects of orientation selectivity.

PDS techniques detect the difference in resonance frequency of an observed spin A for two different states of a dipolar coupled spin B [52]. Assuming only secular contributions, the dipolar coupling Hamiltonian in EPR is given by

$$\widehat{H}_{\mathrm{dd,sec.}} = \omega_{\mathrm{dd}} \widehat{S}_{\mathrm{A},z} \widehat{S}_{\mathrm{B},z} \tag{1}$$

with $\widehat{S}_{i,z}$ being the z-component of spin i and ω_{dd} the strength of the dipolar coupling described by Eq. (2)[19].

$$\omega_{\mathrm{dd}}(r,\theta) = \frac{\mu_0 \mu_{\mathrm{B}}^2 g_{\mathrm{A,eff}} g_{\mathrm{B,eff}}}{4\pi\hbar r^3}\left(1 - 3\cos^2\theta\right) \tag{2}$$

Here, μ_0 is the vacuum permeability, μ_{B} the Bohr magneton, $g_{\mathrm{A,eff}}$ and $g_{\mathrm{B,eff}}$ are the effective g-values of the spins A and B at the given field and frequency and $\hbar$ is the reduced Planck's constant and r is the distance between spins A and B. The angular dependence of the dipolar coupling in EPR is parametrized by the angle θ between the spin-spin vector and the external magnetic field B_0[52]. The effective g-values $g_{i,\mathrm{eff}}$ result from the orientation of the individual spins A and B with respect to the external magnetic field B_0 according to Eq. (3) for spin i in the Bleaney transformation [53].

$$g_{i,\mathrm{eff}}(\theta_i,\phi_i) = \sqrt{g_{i,x}^2 \sin^2\theta_i \cos^2\phi_i + g_{i,y}^2 \sin^2\theta_i \sin^2\phi_i + g_{i,z}^2 \cos^2\theta_i} \tag{3}$$

Here $g_{i,x}$, $g_{i,y}$, and $g_{i,z}$ are the principal values of the g tensor of the spin i and the polar angles θ_i and ϕ_i determine the orientation of B_0 in the g_i-tensor eigenframe.

Experimentally, excitation of A and B spins in the PDS experiments can be performed in two conceptionally different ways [54,55]. 'Single-frequency' schemes that excite both spins, A and B, at the same time by all pulses can be separated from 'pump-probe' schemes that select specific fractions of the spectrum for an observed spin A and a pump spin B. The former group comprises solid-echo based experiments like SIFTER [56] (SIngle Frequency Technique for Refocusing) and DQC [57,58] (Double Quantum Coherence) experiments. They were so far predominantly applied to systems with relatively narrow spectra like trityl or nitroxides, although Cu(II)-Cu(II) DQC distance measurements have been conducted as well [59,60].

In contrast, excitation of all spins simultaneously is technically challenging for systems with broad spectra. For distance determination in such systems, pump-probe experiments, like Double Electron Electron Resonance (DEER),[61,62] also called Pulsed Electron Double Resonance (PELDOR), or Relaxation Induced Dipolar Modulation Enhancement (RIDME) [63] are more commonly applied. Both in DEER and in RIDME, a specific fraction of the spectrum is selected as spin A by the observer pulses. The two techniques differ in the way how the inversion of the spin B is performed. While in DEER inversion of spin B is achieved by a pump pulse at a second frequency, RIDME relies on stochastic relaxation events to flip the coupled spin B. In RIDME, in order for a significant number of B spin flips to occur during the measurement time, the phase-dispersed coherence on spin A is stored in form of a polarization grating for a period T_{mix} called the mixing time. The most commonly used pulse sequences for DEER and RIDME [62,63] are compared in Fig. 1(a and b).

The timing of the pump pulse in DEER and the mixing block in RIDME are varied to probe the difference in resonance frequency of spin A for the two different states of spin B. The difference frequency is detected as an oscillation of the observed echo with a distribution of frequencies $\omega_{\mathrm{dd}}(r,\theta)$. In an ideal powder, all θ values are present weighted by $\sin\theta$. For a specific distance r, the distribu-

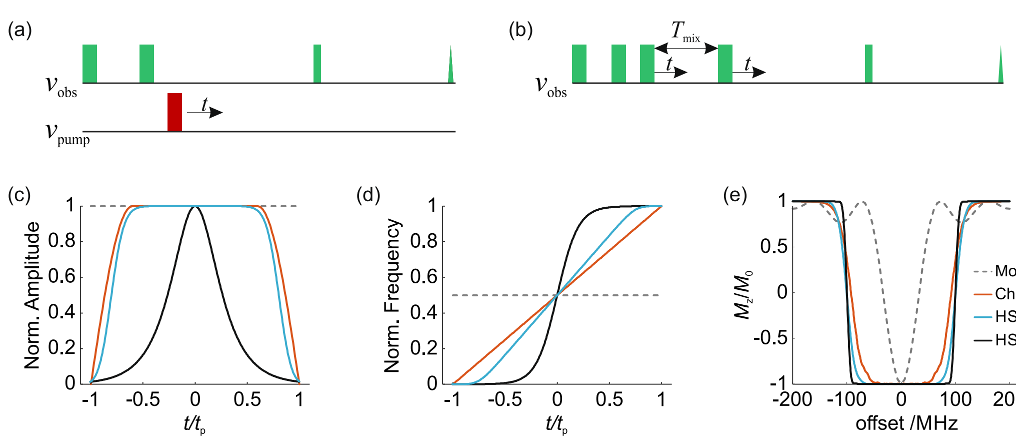

Fig. 1. Pulse sequences for (a) four-pulse DEER [62] and (b) five-pulse RIDME [63]. ν_{obs} indicates the observer frequency, ν_{pump} the frequency for the inversion pulse, t the time increment and T_{mix} the length of the mixing block. Pulse lengths correspond to the versions of the experiments with shaped observer pulses. (c–e) Pulse shapes used for the experiments: Monochromatic (dashed grey), Linear frequency sweep (*chirp*, orange), sech/tanh (HS) pulses of order 6 (blue) and 1 (black). (c) Amplitude modulation. (d) Frequency modulation. (e) Inversion profiles simulated with EasySpin. (For interpretation of the references to colour in this figure legend, the reader is referred to the web version of this article.)

tion of ω_{dd} is described by a Pake pattern. In reality, different conformers can exhibit different spin-spin distances r, resulting in a distance distribution $P(r)$ for the ensemble instead of just a single distance. An ideal dipolar spectrum therefore is a superposition of Pake patterns with each Pake pattern weighted by the probability of the corresponding distance in $P(r)$. If ω_{dd} is not detected for all θ values, or not with the correct weighting, the dipolar spectrum will deviate from a superposition of Pake patterns. This effect is called orientation selection [52].

Applications of Cu(II)–Cu(II) DEER in the past often exploited this effect in order to study the relative orientation of the two g-tensors [64]. Orientation selectivity effects have also been used to monitor relative angles between different structural units in a protein [65]. Distance determination, however, was often complicated by orientation selection caused by the large anisotropy of the Cu(II) spectrum [66–73]. The modulated part of the DEER trace, i.e. the form factor, is multiplied with a smooth decay due to distributed couplings to remote spins. This background contribution can be corrected for by fitting and subsequent division and usually does not interfere with distance distribution determination for sufficiently long DEER traces [74].

Applications of RIDME on nitroxide-Cu(II) systems [75,76] as well as Cu(II)–Cu(II) systems [66] have been demonstrated. Provided that relaxation is uniform enough over the spectrum to avoid different relaxation of the various spin packets during T_{mix}, one can assume complete orientation averaging for the B spins in RIDME experiments and only orientation selection by the observer pulses influences distance distribution determination from RIDME data [66,75,77–79]. For spin $S = 1/2$ systems, RIDME dipolar evolution data can be treated in the same way as data from DEER experiments, i.e. by taking into account only the primary dipolar frequency contributions [77]. Note that for high-spin systems with $S > 1/2$ harmonic overtones of the primary dipolar frequency are introduced [80] and need to be accounted for in data analysis routines [81]. A mathematical description of the RIDME background function has been recently reported [82]. As a rule, the intermolecular background is steeper and more curved in RIDME compared to DEER experiments, as the RIDME background contains additional contributions from nuclear spin diffusion. Generally, the pump excitation bandwidth is larger in RIDME than in DEER which also enhances the intermolecular electron-electron background contribution alongside enhancing modulation depth.

To increase the excitation bandwidth, pulses with frequency and amplitude modulation were introduced recently to EPR [83–85]. Technically this was made possible by home-built implementation of recently developed Arbitrary Waveform Generators (AWG) into existing spectrometers [86–89] or dedicated instruments [90–92]. At first, such frequency-swept excitation was limited to X-band frequencies but soon was extended to Q band, followed by increasingly higher frequencies since. Bandwidths up to 2.5 GHz for excitation and 0.8 GHz for detection have been demonstrated [85]. Recently, frequency-swept excitation has also been used with commercial spectrometers [93].

During a frequency-swept pulse with sufficient field strength B_1, the magnetization effectively stays locked to the effective field in the frame rotating with the instantaneous frequency $f(t)$ [85]. Performance of such an 'adiabatic' pulse can be described in terms of its smallest effective field strength ω_{eff}, i.e. upon passage of the transverse plane, in relation to its sweep rate. This is summarized in the critical adiabaticity Q_{crit} of the pulse defined by Eq. (4)

$$Q_{crit} = \frac{2\pi \cdot \nu_1^2 \cdot t_p}{\Delta f} \tag{4}$$

where ν_1 defines the amplitude of the pulse, t_p the pulse length and Δf the bandwidth. Pulse length requirements for achieving simultaneous refocusing for pulses with time-dispersed excitation have previously been generalized [94].

First implementations of frequency-swept pulses in EPR incremented the instantaneous frequency linearly with time, referred to as *chirp* pulses [87]. The frequency modulation is illustrated in Fig. 1(d). To avoid excitation outside the intended band, the amplitude usually is apodized by a quarter sine, see Fig. 1(c). The resulting inversion profile in subfigure (e), simulated for a two-level system and t_p = 200 ns, achieves 100% inversion around the center of the nominal frequency band of 200 MHz while the frequency flanks lead to partial excitation over ca. 50 MHz. From NMR, pulses modulated by sech/tanh functions, so-called hyperbolic secant or HS1 pulses, are known to provide very well defined inversion bands [95,96]. The simulated inversion profile in Fig. 1(e) indeed demonstrates a much higher selectivity for the HS1 pulse with 100% inversion efficiency over nearly the complete frequency band and very steep frequency flanks. At given maximum amplitude, HS pulses of higher order h, i.e. HSh pulses, provide higher adiabaticity Q_{crit}[97], at the expense of a somewhat less steep frequency flank. This is illustrated in Fig. 1 for a HS1 and HS6 pulse: the amplitude of the HS6 pulse is higher over a larger fraction of the total pulse length t_p which results in a higher Q_{crit}. At the same time, steepness of the simulated frequency flanks of the HS1 pulse outperform the ones of the HS6 pulse in Fig. 1(e). In other words, the order h of HSh pulses provides a parameter to tune the adiabaticity against the steepness of the frequency flank to optimize a given experimental setup [85,98]. In the following, we use the expression *shaped pulse* for any pulse with amplitude and frequency modulation.

Application of an ultra-wideband (UWB) pump pulse, i.e. $\Delta f > 0.5$ GHz, in X-band DEER measurements has been shown to yield large increases in modulation depth and thus sensitivity for a nitroxide-Cu(II) system [87]. Compensation for the instrument response function $\nu_1(f)$ was developed to allow for offset-independent adiabaticity and thus uniform excitation [91]. Applications of UWB pulses at higher frequencies mainly focused on high-spin systems so far: large sensitivity gains for Gd(III)–Gd(III) DEER measurements were achieved by an UWB pump pulse [99,100] and by pre-polarization of the observed central transition by magnetization transfer from $m_S > \frac{1}{2}$ levels [101]. Recently, shaped pulses were employed for RIDME measurements of a nitroxide-Cu(II) system [102]. Determination of Mn(II)–Mn(II) distances allowed for characterization of ATP-fuelled proteins by paramagnetic ion substitution of Mg(II) [33].

Even though compensation of the sweep rate of adiabatic pulses can allow for uniform excitation beyond the resonator bandwidth [91], adiabaticity of the pulses is ultimately limited by the resonator field strength B_1 and Δf_{res}. Furthermore, broadband detection is attenuated by the resonator $\nu_1(f)$-profile. For these reasons, broadband resonators with high and uniform B_1 fields and large Δf_{res} are a field of ongoing development [103–106]. High B_1 fields are of less concern for excitation of high-spin systems due to their larger transition moment. Our recent design of a Q-band resonator based on a loop-gap structure allows for microwave field amplitudes ν_1 > 40 MHz over a range of nearly one GHz [105]. This development set a promising starting point to study potential increases in sensitivity by shaped pulses for distance measurements of a spin 1/2 system with a broad spectrum.

In this study we set out to compare the performance of DEER and RIDME measurements of Cu(II)–Cu(II) systems. In particular, we explore the sensitivity gain by shaped pulses for both experiments. We first characterize relaxation parameters of the bis[Cu(II)-PyMTA] ruler used throughout this work. The performance of different shaped pulses for the given spin system is studied first for 2-pulse echoes in Section 3.2. In DEER measurements, application of shaped pulses for the pump band and the observer band is studied individually and in combination in the Sections 3.3.1 and 3.3.2. Delays in the RIDME experiments are first optimized in Section 3.4.1 before we discuss the application of shaped pulses in Section 3.4.2. We proceed to compare orientation selection in UWB DEER and RIDME for the geometrically constrained system studied here before we conclude the paper with a summary of our findings for both methods.

2. Experimental

2.1. Sample preparation

The syntheses of the Cu(II)-PyMTA complex and the stiff bis[Cu(II)-PyMTA] ruler employed in this study have been described elsewhere [82,105,107,108]. The structure of the Cu(II)-PyMTA complex is shown in Fig. SI 3, the structure of the bis[Cu(II)-PyMTA] ruler in Fig. 10(d). Stock solutions were diluted to final concentrations of 200 μM in a 1:1 (v:v) D_2O/glycerol-d_8 mixture at a pH of ~7. The sample solutions were filled into 1.6 mm (loop-gap resonator) or 3 mm (TE_{102} box resonator) o.d. quartz capillaries and subsequently shock-frozen by immersion into liquid nitrogen.

2.2. EPR measurements

CW X-band EPR spectra were detected using a Bruker Elexsys E500 spectrometer equipped with a Bruker Elexsys Super High Q probehead and a nitrogen flow cryostat. Measurements were performed at 140 K, 100 kHz field modulation, 140 mT field sweep width, 0.4 mT modulation amplitude, and 0.2 mW microwave power (30 dB attenuation). The time constant was 40.96 ms and the conversion time 327.68 ms.

Pulsed EPR experiments in Q band were acquired on two different spectrometers. A commercial Bruker Elexsys E580 spectrometer, which can be used with a homemade AWG extension to allow for broadband pulses at a second frequency band [87], or a home-built spectrometer based on a Keysight Arbitrary Waveform Generator (AWG) [91] with a high-power Q-band extension [109]. Both spectrometers were equipped with TWT amplifiers with 200 W nominal power and either a home-built TE_{102} box cavity operating at about 34.5 GHz [110] allowing for 3 mm samples or a broadband resonator with a pent loop gap design for 1.6 mm samples was used with the coupler set to provide the lowest possible Q-value [105]. W-band EPR experiments were performed on a Bruker Elexsys E680 X-/W-Band spectrometer operating at roughly 94 GHz with a home-built W-band microwave bridge and 2 W solid-state amplifier. The spectrometer was equipped with a Bruker TE_{011} resonator. X-band pulse EPR measurements were performed on our home-built AWG spectrometer [91] with a commercial MS3 resonator (Bruker). A helium flow cryostat (ER 4118 CF, Oxford Instruments) was used to adjust and stabilize the measurement temperature.

Echo-detected field-swept EPR spectra were acquired using the Hahn-echo pulse sequence $\pi/2-\tau-\pi-\tau$ with a pulse length t_p of 12 ns or 16 ns for the $\pi/2$ pulse. The length of the π-pulse was set to $2t_p$. The interpulse delay τ was set to 400 ns. Transverse relaxation was studied using the same pulse sequence, where the interpulse delay τ was incremented starting from 400 ns. Longitudinal relaxation measurements were performed using an inversion recovery sequence $\pi-T-\pi/2-\tau-\pi-\tau$ with hard inversion by the first π-pulse of length 12 ns, and a soft detection scheme with pulse lengths of 60 ns for the $\pi/2$ and 120 ns for the π-pulse. τ was set to 400 ns. The delay T was incremented starting from 1 μs.

RIDME data were acquired using the refocused five pulse RIDME experiment $\frac{\pi}{2}-\tau_1-\pi-(\tau_1+t)-\frac{\pi}{2}-T_{\mathrm{mix}}-\frac{\pi}{2}-(\tau_2-t)-\pi-\tau_2$, illustrated in Fig. 1. If not specified differently, $\pi/2$-pulses were set to 12 ns and π-pulses to 24 ns. The interpulse delays were set to τ_1 = 400 ns and τ_2 = 5 μs while t was incremented starting at −120 ns in steps of 16 ns. The mixing time is given by T_{mix} and set to values between 25 and 400 μs. In the two-point optimization it was varied from 1 to 600 μs in steps of 2 μs to study its influence on the signal evolution. To remove echo crossings and phase offsets, an eight-step phase cycle was used [63]. Nuclear modulation averaging was performed according to Ref. [111]. Unless otherwise specified, RIDME data were collected on the Bruker Elexsys E580 spectrometer equipped with a home-built TE_{102} box cavity for oversized samples [110].

DEER measurements were performed with the dead-time free 4-pulse version of the experiment [62] $\frac{\pi}{2}_{\mathrm{obs}}-\tau_1-\pi_{\mathrm{obs}}-(\tau_1+t)-\pi_{\mathrm{pump}}-(\tau_2-t)-\pi_{\mathrm{obs}}-\tau_2$ where τ_1 was set to 550 ns, τ_2 to 5 μs and t was varied in steps of 16 ns. Nuclear modulations were averaged by varying τ_1 in 8 steps of 16 ns. Unless otherwise specified, DEER measurements were performed on the home-built spectrometer using the broadband resonator with a pent loop-gap design. Phase cycling for 4-pulse DEER with a coherent pump pulse channel was performed as described by Tait and Stoll [112]: A 32-step phase cycle was used with [+x −x] on the $\frac{\pi}{2}$-pulse, [+x +y −x −y] on the first observer π-pulse and [+x +y −x −y] on the pump pulse. On the Bruker Elexsys E580 spectrometer with an incoherent pump pulse channel, a two-step phase cycle consisting of [+x −x] on the $\frac{\pi}{2}$-pulse was applied.

The sweep rate of shaped pulses was compensated by the $\nu_1(f)$ profile of the resonator to achieve uniform excitation [91] which was measured in each session. The non-linear amplification by the excitation chain was characterized as described previously [91] and used for pulse compensation. Inversion efficiencies were measured as described in Ref. [91]. UWB pump pulses were employed at the full available amplitude. Shaped observer pulses had length ratios 2:1 for 2-pulse echoes, 2:2:1 for refocused echoes and the DEER observer subsequence and 2:2:2:2:1 for the refocused virtual echoes detected in the RIDME sequence in order to cancel phase shifts [94]. The adiabaticity of the observer pulses was set by sweeping the amplitude of each pulse and selecting the amplitude for maximum echo intensity. The sweep range and direction was the same for all observer pulses, from low to high frequency. The observer frequency band was centered in the 1–2 GHz detection window of the digitizer. The local oscillator (LO)-frequency was adjusted such that the pulses were located centered around the centre of the resonator at resonance frequency f_0. Experiments with shaped observer pulses with a bandwidth of 0.5–0.9 GHz were evaluated by integration over 3 ns (six datapoints) of the echo transients. The frequency offset between observer and pump pulses is defined from pulse edge to pulse edge, where only the two inner (closest) pulse edges of observer and pump pulses are considered.

An optimization of the pump pulse parameters in DEER measurements was performed as described previously [91]. The delay τ_2 was set to 2 μs and two points were measured with $t=\tau_1$ and $t=\tau_1+1$ μs, respectively. For details regarding the setups for all DEER measurements, see Table SI 3 in SI.

All RIDME and DEER traces presented in the sensitivity comparison were recorded with the same measurement time of ca. 1.5 h at 20 K with a shot repetition time of 750 μs.

2.3. Data analysis

Relaxation times. Data were analyzed and processed with home-written MATLAB (The MathWorks Inc., Natick, MA, USA) scripts. Inversion recovery traces were offset-corrected, sign-inverted and subsequently fitted by stretched exponential functions of the form

$c \cdot \exp\left(-(t/T_1)^x\right)$ using nonlinear least-squares fitting. Longitudinal relaxation times T_1 were extracted as fit parameters. Hahn echo decay traces were offset-corrected by removing a (weak) constant offset from the last 20 data points. The data were then fitted by stretched exponential functions of the form $c \cdot \exp\left(-(t/T_m)^x\right)$ using nonlinear least-squares fitting. Fitting errors were extracted from the 95% confidence intervals of the fit. However, we found that experimental uncertainties introduced by the dead time as well as pulse settings can cause larger variation of T_m up to 8%.

Processing of PDS data. RIDME and DEER data were processed with DeerAnalysis.[74] For background correction, the dimension of an exponential background decay was fit to the DEER and RIDME data. Note that this resulted in different background dimensionality for the two methods. Subsequently, the experimental trace was divided by the background fit and normalized. Dipolar spectra were obtained after background correction by Fourier Transform and normalised to their integral in DeerAnalysis.

Extraction of noise. Determination of noise levels as the root mean squared deviation (rmsd) between time or frequency domain fits and experimental data – as is often used as noise estimate – was disturbed by differences due to orientation selection for our data. Instead, noise levels were determined from the outer halves of the dipolar frequency spectrum. White noise of time-domain data is distributed equally over the (dipolar) frequency domain and in this case it is possible to extract the noise independently from the quality of the fit. In the data presented, a slight frequency dependence of the noise level is observed in frequency domain due to the time dependence of the noise in the primary data. The noise is thus not strictly white. However, using different fractions of the frequency domain data in the noise analysis did not influence the qualitative findings. Consequently, the noise level $n_{\mathrm{l,FT}}$ was determined from the rmsd between the dipolar spectrum and the zero baseline in the outer halves of the frequency domain data. Because the dipolar spectra were normalized to their integral, the noise level extracted in this way is already inversely scaled by the modulation depth λ and the sensitivity η can be directly calculated as the inverse of $n_{\mathrm{l,FT}}$. To estimate the noise level $n_{\mathrm{l,M}}$ on the time domain traces, i.e. independent of the modulation depth, the rmsd between the moving average of 15 data points and the experimental traces was calculated. In this case, the sensitivity η_M corresponds to $\lambda/n_{\mathrm{l,M}}$.

3. Results and discussion

3.1. Characterization of Cu(II)-PyMTA for dipolar spectroscopy

Relaxation rates are important parameters in pulsed dipolar experiments. The transverse relaxation rate limits the maximal detectable trace length and thus the distances that can be extracted. In this respect a long phase memory time T_m is beneficial and T_m can be significantly prolonged by solvent deuteration [113]. Equilibrium magnetization builds up with the longitudinal relaxation rate due to spin-lattice interactions. It thereby sets an upper limit for the repetition rate of the EPR experiment. For a given measurement time, it thus also constrains the SNR. Further, in the case of RIDME experiments spontaneous spin flips of the B spins during the mixing block introduce the dipolar modulation to the RIDME signal. The smaller $T_{1,\mathrm{B}}$, the higher the probability of a spin flip. However, if $T_1 \sim T_\mathrm{m}$ a significant number of spontaneous flips of A spins will occur during the transverse evolution period reducing the modulation depth in dipolar spectroscopy. Further in the case of RIDME experiments, the electron coherences that are not transferred to polarization by the first $\pi/2$ pulse of the RIDME mixing block will further contribute additional, unwanted echoes to the RIDME signal evolution if $T_{\mathrm{mix}} \leqslant T_\mathrm{m}$. Accordingly, a ratio of T_1/T_m of about 5 was considered to be best suited for metal-metal RIDME experiments [114]. The temperature and field dependence of the relaxation rates makes these parameters factors to consider in the optimization of measurement conditions for a certain spin system. Fig. 2 shows the extracted T_m and T_1 times for the bis[Cu(II)-PyMTA] ruler in the range of 10–30 K. It can be seen that for decreasing temperatures ⩽15 K, the T_1 times become significantly longer, which leads to an increase in measurement time due to long repetition rates at the same SNR. On the other hand, transverse relaxation increases more gradually. In the studied system at 20 K and in Q band, the signal intensity is decayed to 10% of its initial value at 18 μs, which serves as an estimate of the upper distance limit assuming the background decay can be neglected, e.g. in DEER at very low spin concentration. This corresponds to a full period of the dipolar coupling frequency for distances up to 10 nm. For temperatures ⩾20 K, the T_1/T_m ratio is in a reasonable range for RIDME measurements. Thus, a measurement temperature of 20 K was chosen for all distance measurements as best compromise between long T_m, experimental repetition rate and T_1/T_m ratio. Note that at higher measurement temperatures of 25 K the T_1/T_m ratio further decreases to the optimal value of ~5, which may be more optimal for RIDME measurements if the phase memory time remains sufficiently long. However, this was not tested experimentally here.

The qualitative findings for the relaxation rates are the same in Q and W band. While the number of detectable spins decreases with increasing microwave frequency, the situation is more complex for concentration sensitivity and in pulse EPR experiments with limited bandwidth. Significant broadening of the Cu(II) spectrum occurs while the excitation bandwidth remains similar (between X and Q band) or even decreases (for W band) due to technical difficulties to provide and apply amplifier technology with similar output power in W band. This leads to a loss in SNR as only a smaller fraction of the spectrum can be detected. Thus,

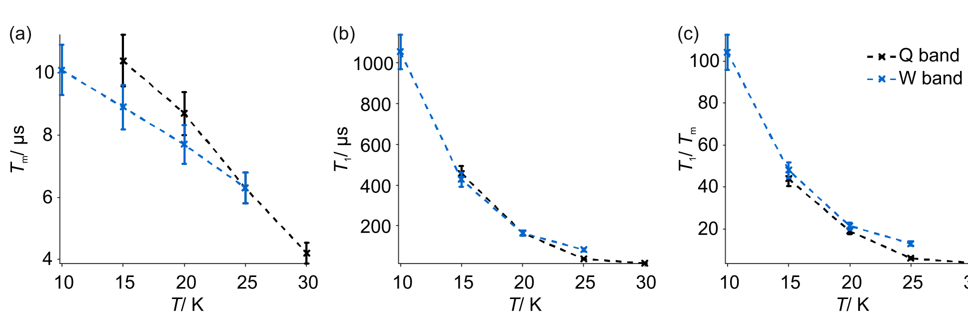

Fig. 2. Relaxation times of bis[Cu(II)-PyMTA] ruler in Q band (black crosses) and W band (blue crosses). The dashed lines are guides for the eye. (a) Phase memory time T_m and (b) longitudinal relaxation time T_1. (c) Division of longitudinal by transverse relaxation T_1/T_m. The relaxation times are estimated from fitting stretched exponential functions of the form $c \cdot \exp\left(-t/T_i\right)^x$. The fitting parameters x and T_i are provided in the SI. (For interpretation of the references to colour in this figure legend, the reader is referred to the web version of this article.)

most of the experiments were performed in Q band. In order to excite a larger fraction of the Cu(II) spectrum, the performance of DEER experiments using shaped pulses was also studied in X band.

3.2. Shaped pulses

3.2.1. Performance of shaped pulses

In Fig. 3(a), the Q-band EPR spectrum of the bis[Cu(II)-PyMTA] ruler is shown cast on a frequency axis. As is common for the EPR spectra of metal centers, the spectrum spans several GHz, in this case more than 4 GHz. In comparison, most commercial resonators exhibit a narrow mode $B_1(f)$ and the available resonator bandwidth Δf_{res} is usually below hundred MHz even at complete overcoupling. As mentioned already in the introduction, limitations in $\nu_1(f)$ and bandwidth Δf_{res} by the resonator ultimately restrict the adiabaticity of the pulses as well as broadband detection. The $\nu_1(f)$ profile (red) of a recently developed broadband resonator [105] is overlaid onto the spectrum (black) in Fig. 3(a). Fast nutation frequencies $\nu_1 > 40$ MHz, are available over a range of nearly one GHz. With

$$\frac{\nu_1 \cdot h}{g \cdot \mu_B} = B_1 \tag{5}$$

this corresponds to $B_1 > 1.43$ mT. Such high B_1 fields over such a large resonator bandwidth Δf_{res} are highly promising for measurements of spin 1/2 systems using shaped pulses. We already demonstrated recently [105] that the gain in sensitivity for Cu(II)–Cu(II) DEER measurements using a HS6 pump pulse in this resonator is larger than in a home-built resonator with narrower resonator bandwidth [110].

Inversion efficiencies $E = (M_0 - M_z)/2M_0$, with M_0 being the equilibrium magnetization and M_z being the longitudinal magnetization along the z-direction, measured on the bis[Cu(II)-PyMTA] ruler for linear frequency sweeps (*chirps*) covering different frequency bandwidths Δf are shown in Fig. 3(b). For all pulses, the frequency flanks are well defined and excitation in the specified frequency band is largely uniform. A slightly lower inversion efficiency is observed for a pulse bandwidth Δf of 0.9 GHz. This is expected, as according to Eq. (4) the adiabaticity at a broader sweep range Δf is lower, see Table 1, which in turn decreases the inversion efficiency. However, the inversion efficiency does not exceed 70% in any case. This is well below the expected inversion efficiency which should be 100% for an ideal system and $Q_{crit} > 5$.

We tested if this loss in inversion efficiency is caused by the dipolar coupling in the bis[Cu(II)-PyMTA] ruler by performing the same experiments on the Cu(II)-PyMTA complex. The same frequency-dependent inversion profiles were obtained as shown in Fig. SI 3 in the Supporting Information. We currently do not fully understand what limits the inversion efficiency. Spin dynamics during adiabatic pulses differs from the one upon simultaneous excitation of all transitions by monochromatic pulses. The time-dependence of excitation can lead to coherence transfer effects if transitions with slightly different frequencies are passed consecutively [94]. This resulted for example in the observation of additional peaks in 3-pulse Electron Spin Echo Envelope Modulation (ESEEM) spectra that were dependent on the sweep direction [115]. However, the maximal inversion achieved by monochromatic pulses is with less than 80% for this spin system also significantly below the expected level. This suggests that the loss in inversion efficiency for the Cu(II)-PyMTA complex is not dominated by coherence transfer effects resulting from dipolar coupling.

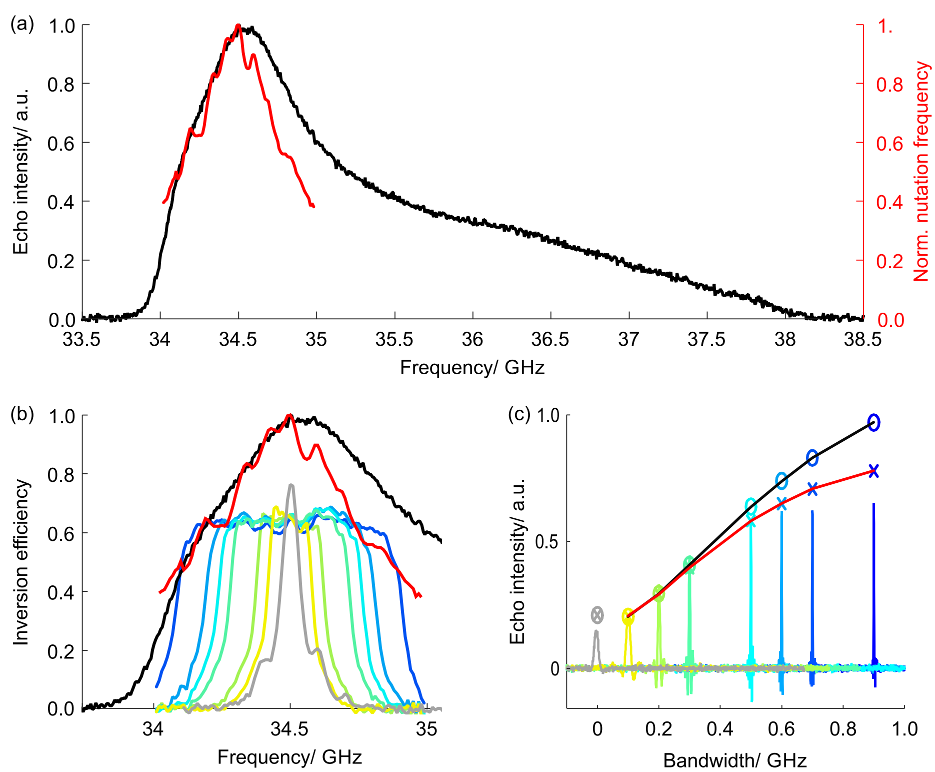

Fig. 3. (a) Overlay of the resonator $\nu_1(f)$-profile (red) of the broadband resonator on the echo-detected field sweep spectrum $I(f)$ (black). (b) Inversion efficiencies $E(f)$ for chirp pulses of different pulse bandwidth Δf (coloured lines) and of a monochromatic 12 ns pulse (grey), with $I(f)$ and $\nu_1(f)$ overlaid. (c) Echo transients for 2-pulse chirp echoes, centered around 0 and shifted according to the pulse bandwidth Δf, with the same color code as in (a) and (b). As expectation for the maximal echo intensity, we compare the normalized integrals $\int E(f) \cdot I(f)\, df$ (circles) and $\int E(f) \cdot I(f) \cdot \nu_1(f)\, df$ (shown as x). The predicted echo intensities were scaled so that the prediction for a 2-pulse echo with 0.1 GHz chirps agrees with the experimentally observed echo intensity. Lines connecting the circles (black) and x-symbols (red) are guides for the eye. (For interpretation of the references to colour in this figure legend, the reader is referred to the web version of this article.)

Table 1
Predicted adiabaticities of the shaped observer pulses used for the 2-pulse echoes in Fig. 3 (chirp pulses) and for HS pulses of order 6 at the same pulse bandwidth Δf.

Pulse bandwidth Δf/GHz	0.9	0.7	0.6	0.5	0.3	0.2	0.1
Adiabaticity Q_{crit} for chirp pulses	2.4	4.1	5.2	7.1	14.7	23.6	49.5
Adiabaticity Q_{crit} for HS6 pulses	1.4	2.6	3.4	4.5	10.4	17.3	35.8

Instead it could be a consequence of the hyperfine coupling and excitation of forbidden transitions. Preliminary tests on E'-centers in γ-irradiated quartz glass, a system that does not exhibit hyperfine couplings, showed that 100% inversion can be achieved on our experimental setup. Note that for the Cu(II)-PyMTA complex it might be possible to achieve higher inversion efficiencies if the sweep rates of the pulses are not compensated for the resonator $\nu_1(f)$ profile. However, this gain in peak inversion efficiency would be at the expense of uniformity of inversion. Investigation of these effects is deferred to a dedicated study. Here, we proceeded to the comparison of methods based on the currently achievable performance.

To summarize, broadband pulses with well defined frequency bands and largely uniform inversion profiles are available in our experimental setup using the broadband resonator. However, the level of inversion is limited to 65–75% for the Cu(II)-PyMTA complex due to reasons which have yet to be understood.

3.2.2. Shaped observer pulses

To test the performance of shaped pulses for the observer subsequences in DEER and RIDME experiments, we first consider the simpler case of a 2-pulse echo. In Fig. 3(c), echo transients resulting for 2-pulse echoes of chirp pulses of different Δf are shown with the same color code as the pulse profiles in Fig. 3(b). Simultaneous refocusing is achieved by adjusting pulse lengths to avoid phase dispersion [94]. Two observations can be made: (i.) The broader the excited frequency range, the narrower the observed echo in time domain is. (ii.) The peak echo intensity increases with an increased fraction of the spectrum being covered.

(i) A narrower echo is expected for simultaneous refocusing of a broader range of frequencies: before and after the exact time of refocusing, the different frequency contributions will lead to destructive interference. In a linear approximation, the shape of the echo transient is the Fourier Transform of the product of the excitation profile with the spectral lineshape. With increasing pulse bandwidth (range of frequencies), destructive interference takes place closer in time to the refocusing point. When comparing shaped pulses to monochromatic pulses, shortened 2-pulse echoes were already observed for nitroxide samples [91,116] as well as for X-band measurements of the hexaaqua Cu(II) complex $[Cu(H_2O)_6]^{2+}$[91]. Due to the narrower spectrum in both cases, the effect was less pronounced. Here, we observed a systematic shortening of the echo with increasing excitation bandwidth as it would be expected from theory. It follows, that the echo integration window has to be adjusted individually based on the excited frequency range for experiments with shaped observer pulses evaluated by echo integration.

(ii) For increasing pulse bandwidth Δf of the pulses, the peak echo intensity increases approximately linear with the pulse bandwidth for $\Delta f < 0.5$ GHz before it saturates for broader Δf. The peak echo intensity corresponds to the number of excited spins which in turn corresponds to the integral over the product of the excitation efficiency profiles $E(f)$ of the pulses and the spectrum $I(f)$. We compared the integrals $\int E(f) \cdot I(f) df$ for each pulse bandwidth Δf to the maximal value of the averaged echo transient in Fig. 3(c). The intensity value is of arbitrary unit. We thus had to choose a reference point for comparison of the predicted echo integrals and the maximal value of the echo transients. The predicted echo integral for a 2-pulse echo of a 0.1 GHz chirp was calculated from the pulse profile of such a pulse, shown in yellow in Fig. 3(b), and used to determine a scaling factor. Note that this scaling factor only represents a rough estimate so that we can discuss trends but not absolute values. The predicted echo intensities follow the initial trend of increasing echo intensity for $\Delta f < 0.5$ GHz. However, the effect of saturation at broader pulse bandwidth Δf is not reproduced by the calculated echo intensities.
The frequency-dependence of the resonator attenuates the echo contributions with frequencies further away from the center of the resonator mode f_0. Compensation of the sweep rate of the pulses should alleviate attenuation by the resonator for excitation, but not for detection. We tried to mimick this attenuation by including $\nu_1(f)$, which is proportional to the frequency dependence of detection efficiency, into the calculation as $\int E(f) \cdot I(f) \cdot \nu_1(f)\, df$. The echo intensities predicted with inclusion of $\nu_1(f)$ are marked by x-symbols in Fig. 3(c) and connected by a red line as guide for the eye. For broad pulse bandwidth Δf, attenuation of the increase in peak echo intensity is observed albeit less strongly than in the experimental data. This suggests that also other effects contribute to the reduction in echo intensity for broad Δf. Some of these losses in echo intensity might result from instantaneous diffusion which is expected to increase if a larger fraction of the spectrum is excited. Interestingly, the predicted echo intensities for the Cu(II)-PyMTA complex match the experimental ones better (see Fig. SI 3). This might indicate that some of the echo loss at higher Δf for the bis[Cu(II)-PyMTA] ruler is due to coherence transfer to forbidden transitions, which was predicted theoretically for a system of two dipolar coupled spins.[94] However, as the scaling of the echo intensities is arbitrary, the agreement for the Cu(II)-PyMTA complex has to be interpreted with caution.

We further tested the influence of pulse length, pulse shape and compensation for the $\nu_1(f)$ profile of the resonator on the peak echo intensity, see Figs. SI 4 and SI 5 in the Supporting Information. We found similar performance for HS6 pulses and chirps. For shaped pulses with different parameters, the optimal pulse amplitudes were found to be different, as expected due to differences in adiabaticity. However, the maximal peak echo intensity was found to remain very similar provided a sufficient adiabaticity can be reached for the given pulse length and shape. We therefore conclude that the peak echo intensity is not limited due to these technical parameters.

Based on these experiments, we chose HS6 pulses for the observer part of the pulse sequence in the following DEER and RIDME measurements as they were found to provide robustly a high adiabaticity and still maintain a reasonable steepness of the frequency flanks and thus well defined excitation profiles. With HS6 pulses, the highest echo intensities were found for a pulse bandwidth Δf of 0.5 GHz when integrating 3 ns of the echo transients.

Analogous results as in these optimizations regarding 2-pulse echoes were obtained for the intensity of a refocused echo, which corresponds to the observer subsequence of the DEER experiment (data not shown).

3.3. DEER experiments with wideband pulses

3.3.1. Shaped pump pulses

Shaped pulses were employed as pump pulses in DEER measurements with monochromatic observer pulses. In order to find optimal parameters for the shaped pump pulse, a procedure adapted from Doll et al. [91] was used: two points of the DEER trace $S(t)$ were recorded while pump pulse parameters were varied. The timings of the pump pulse corresponded to the maximal echo intensity of the DEER trace, i.e. the zero time, and to the first local minimum of the DEER trace, respectively. The difference between the two data points serves as sensitivity estimate because $S(0) - S(t) = S(t) \cdot \lambda$. Note that this 2-point procedure can lead to distorted results for systems with strongly correlated geometry if the first local minimum is artificially lowered by orientation selection effects. However, the measurements presented here were detected at the maximum of the Cu(II) spectrum where many orientations contribute so that orientation selection effects are reduced [73].

Optimization of the offset and pulse bandwidth Δf (frequency range) were carried out for different shapes and lengths of the pump pulse. In Fig. 4, the results for a HS pump pulse of order 1 and 6 and length of 250 ns, as well as for a 100 ns-long HS6 pulse are shown to visualize two general trends that were observed:

(i.) The optimal pulse bandwidth Δf is larger with increasing HS order and with increasing pulse length. The former effect is nicely illustrated by the difference in optimal Δf for the HS1 and HS6 pulse of the same length of 250 ns in Fig. 4(a) and (c): 0.8 GHz and 1.2 GHz, respectively. The latter effect is observed when increasing the pulse length of a HS6 from 100 ns to 250 ns: the optimal Δf changes from 0.8 GHz to 1.2 GHz, cf. Fig. 4(b) and (c). Both observations agree with expectations: A HS pulse of higher order has a higher adiabaticity [117]. And a longer pulse can maintain a high adiabaticity Q_{crit} at higher Δf based on Eq. (4). However, the length of the pump pulse in DEER is limited by the shortest distance r_{min} contributing to the distance distribution: the time-dependence of inversion by the shaped pump pulse can lead to an artificial broadening of the distance peaks if the length of the pump pulse t_{p} is $> \frac{T_{\mathrm{dd}}}{4}$ where T_{dd} is the dipolar oscillation period [99]. The pulse lengths 100 ns and 250 ns were chosen to model distance measurements of systems with a shortest distance contribution $r_{\mathrm{min}} > 2.75$ nm and $r_{\mathrm{min}} > 3.73$ nm, respectively.
From this optimization, we conclude that the modulation depth and thus sensitivity of DEER measurements with monochromatic observer and shaped pump pulses increases with Δf, HS order and length of the pump pulse, while the shortest distance to be detected limits the pump pulse length.

(ii.) The optimal frequency offset between observer and pump pulse correlates with the steepness of the frequency flank of the pump pulse. A lower order of the HS pulse leads to a more defined frequency flank, see Fig. 1(e). Similarly, an increased pulse length helps defining the frequency flank better. A more defined frequency flank in turn decreases the optimal offset and thus also allows for a smaller offset if this is required for the spectroscopic question at hand.

Further note that the experiments presented in Fig. 4 were performed with the sweep rate of the pump pulses adapted to the $\nu_1(f)$ profile of the resonator. We compared these results to experiments without compensation and found the same trends (data not shown). Note however, that the higher uniformity of the compensated pulses should simplify interpretation of the DEER data, in particular if orientation selection must be considered.

In summary, we found that an individual optimization of the pump pulse parameters for a given combination of spectrometer, resonator and spin system is advantageous. HS6 pulses of length restricted by $t_{\mathrm{p}} < \frac{T_{\mathrm{dd}}}{4}$ appear generally to be a robust choice for a broad range of 'optimal' pulse bandwidth Δf. We expect these observations to hold true not only for DEER measurements between Cu(II) centers but between any two spin 1/2 systems with broad and potentially overlapping spectra.

The optimized pump pulses were applied in DEER measurements with monochromatic observer pulses, see Fig. 5(a). The traces were compared to a DEER measurement with the shortest monochromatic pulse of 7 ns length available in the center of the Q-band broadband resonator as pump pulse which results in a modulation depth λ of 6%. The modulation depth λ was significantly increased to 17% for a HS1 pump pulse of length 250 ns. With a HS6 pulse of the same length, 27% modulation depth were achieved. Reducing the length of a HS6 pump pulse to 100 ns still yields λ = 20%. These observations roughly correspond to the predictions made from the 2-point optimizations, cf. Fig. 4. As discussed there already, a shorter pump pulse has to be used for shorter r_{min}. These DEER traces therefore confirm that the maximal sensitivity gain by shaping the pump pulse will be lower if shorter distances r_{min} are of interest.

The noise level $n_{\mathrm{l,M}}$ and initial signal intensity $S(0)$ of the individual DEER traces appear to be rather similar between the traces with different pump pulses. Thus the sensitivity η for distance determination is strongly increased in the DEER traces with HS6 pump pulses in comparison to the monochromatic pump pulse. For details see Table SI 5 in the SI.

In Fig. 5(b), the pulse bandwidth Δf is cast on a field axis and overlaid on the echo-detected field sweep. From this direct

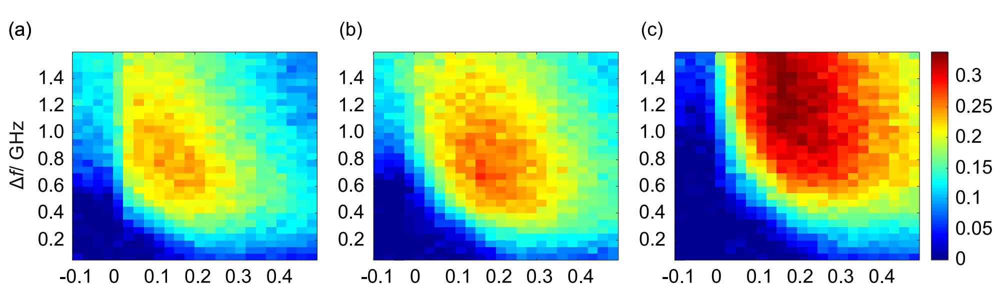

Fig. 4. 2-point optimization for Q-band DEER experiments with pump pulses of different shape and length: (a) HS1 250 ns, (b) HS6 100 ns, (c) HS6 250 ns. Observer pulses were monochromatic (12 ns) and placed at the maximum of the spectrum. The difference between the intensity at t_0 and $t_0 + 1$ µs is plotted, normalized to the maximal echo intensity at t_0. For a pump pulse of higher HS order or longer duration, broader pulse bandwidths Δf are optimal due to the higher adiabaticity.

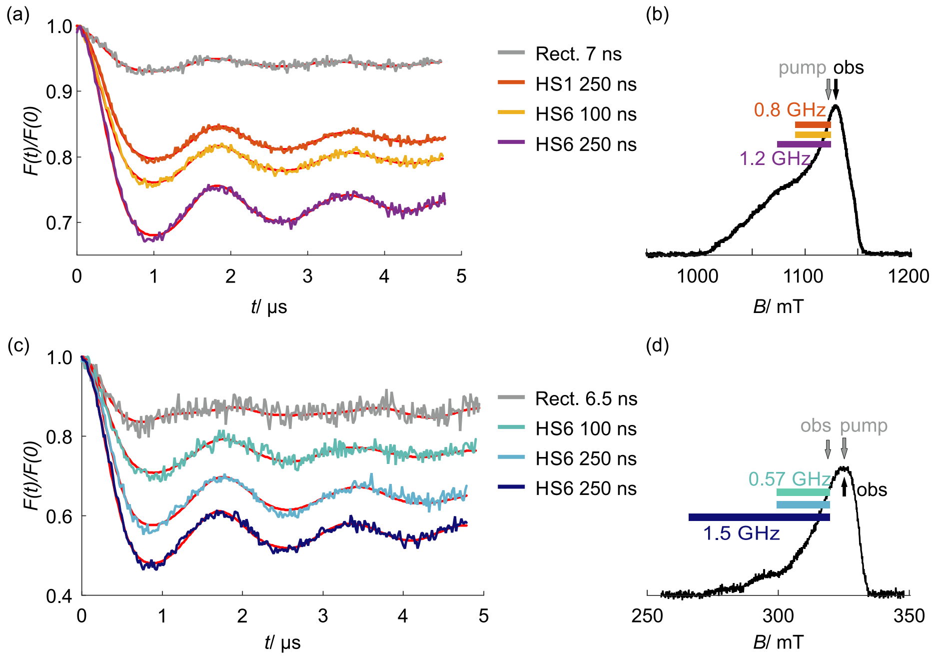

Fig. 5. DEER with UWB pump pulses. The monochromatic 12/12 ns observer pulses were placed at the maximum of the spectrum. (a) Q-band DEER background-corrected form factors, (b) Q-band echo-detected field sweep with ranges covered by the pulses indicated, (c) X-band DEER background-corrected form factors, (d) X-band echo-detected field sweep with pulse ranges indicated. Note that for X-band DEER with monochromatic pump pulse the pump frequency was placed on B_{max} and the observer towards lower field. The modulation depth is increased strongly by the application of the shaped pump pulse, in comparison to the rectangular pump pulse shown in grey. (a and c) Form factor fits are overlaid in red. (For interpretation of the references to colour in this figure legend, the reader is referred to the web version of this article.)

comparison it is clear that many more spins are included into the experiment by the use of the HS compared to the monochromatic pump pulse. However, a significant fraction of the spins is not yet excited in the Q-band DEER traces. For the bis[Cu(II)-PyMTA] ruler studied here, this manifests in residual orientation selection: the fit corresponding to a superposition of Pake patterns and the experimental traces deviate slightly for dipolar evolution times between 0.9 and 1.1 µs in Fig. 5(a). Orientation selection is discussed in detail in Section 3.5. For now it suffices to note that not all spins take part in the Q-band experiments with shaped pump pulses. However, a much larger fraction of all spins is excited than in the case of a monochromatic pump pulse.

In X band, the spectrum of the Cu(II)-PyMTA complex spans about 80 mT, which is less than half of the spectral width in Q band. In the following, we explore what fraction of the narrower X-band spectrum can be included into the DEER experiment by a shaped pump pulse.

A significant fraction of the spectrum can be excited in X band already by the shortest available monochromatic pulse of 6.5 ns (−0.15 GHz) pumping on B_{max}. This in turn increases λ to 14%, shown as grey trace in Fig. 5(c). However, the noise level $n_{l,M}$ in the time domain data is slightly higher in the X-band than Q-band DEER traces as concentration sensitivity is higher at the higher frequency. These two effects partly compensate each other with respect to the sensitivity η of DEER measurements, resulting in similar sensitivity for DEER with a monochromatic pump pulse in X band and in Q band, see Table SI 5 in the SI.

X-band DEER measurements with shaped pump pulse were performed with the monochromatic observer pulses positioned at B_{max}. A trace recorded with a HS6 pump pulse of 100 ns length and 0.57 GHz bandwidth Δf, is compared to a DEER trace with a pump pulse of the same Δf but a length of 250 ns in green and light blue in Fig. 5(c). The modulation depth was drastically increased to 24% and 36% for the 100 ns and 250 ns-long HS6 pump pulse, respectively. From the overlay of the bandwidth Δf of the pulses and the echo-detected field sweep spectrum in Fig. 5(d) it becomes clear that a much larger fraction of the spins take part in the experiment. However, the fit by a superposition of Pake patterns in Fig. 5 (c) still deviates from the experimental data for dipolar evolution times of 0.9–1.1 µs. This residual orientation selection can be reduced by increasing the bandwidth Δf of the pump pulse to 1.5 GHz, i.e. covering the entire low-field shoulder of the spectrum. The corresponding DEER trace is shown dark blue in Fig. 5(c). The change in the shape of the DEER data – including an increase in modulation depth to 44% – proves that a different set of pumped spins participates in the experiment. Indeed, the shape of the form factor agrees much better with the fit by a superposition of Pake patterns. Note also that this modulation depth is similar to the one achieved for nitroxide pairs with monochromatic pulses.

Despite the increased noise level $n_{l,M}$ in X band compared to Q band, we found the sensitivity η of X-band DEER with shaped pump pulses to be similar to the one of Q-band DEER due to the increased modulation depth λ, see Table SI 5 in SI.

To summarize, we found a strong increase in modulation depth and thus sensitivity by substituting the monochromatic pump pulse by a shaped one for DEER experiments both in X and Q band. With a 250 ns pump pulse, corresponding to $r_{min} > 3.73$ nm, the increase in the fraction of the spectrum excited by the pump pulse resulted in even larger sensitivity gains. Due to the narrower spectrum in X band, it was possible to include nearly the whole spectrum in the experiment. The gain in coupled spin pairs cancelled the lower concentration sensitivity of X vs. Q band and lead to a similar sensitivity of X-band and Q-band DEER.

3.3.2. All pulses shaped

The shaped observer pulses were combined with a shaped pump pulse for DEER measurements. In order to assess the individual gain by sweeping the frequency of either the observer or the pump band, we investigated all possible combinations, i.e. monochromatic observer pulses with monochromatic pump pulse

(M_oM_p), monochromatic observer pulses and shaped pump pulse (M_oS_p), shaped observer pulses and monochromatic pump pulse (S_oM_p) and shaped observer pulses with shaped pump pulse (S_oS_p). The traces are compared in Fig. 6(a).

All shaped pulses had a width of $\Delta f = 0.9$ GHz and were placed on one side of the resonator each: the observer pulse frequency range began 50 MHz above and the pump pulse frequency range began 50 MHz below the resonator center f_0 at $B = B_{max} - 10.4$ mT, respectively. The regions of the spectrum covered by the individual pulses are cast on a field axis and overlaid over the echo-detected field sweep in Fig. 6(b). They were kept constant between all traces, so that for example the shaped pump pulse (S_p) had the same frequency range in the M_oS_p and S_oS_p setup. Note that this corresponds to a pulse setup with lower sensitivity for M_oM_p than setting the observer position onto the spectral maximum as was done for the measurements in Fig. 5(a).

Analogously to the observations made above in Fig. 5(a), the M_oS_p setup resulted in a large gain in modulation depth λ over the M_oM_p setup from 4% to 28%. In contrast, the S_oM_p setup did not result in a significant increase in λ (5%). Both these observations agree with considerations of orientation selection for geometrically correlated systems: The observer frequency selects the orientation(s) of the molecular system with respect to the external magnetic field B_0. The pump pulse induces a contribution to the modulation only if the resonance frequency of the coupled spin for this orientation of the molecular axis system corresponds to the pump pulse frequency band. In other words, the pump frequency range determines λ within the observer-selected molecular frame. For the M_oS_p setup this corresponds to an increase in λ as the range in pump frequencies is broadened, which increases the probability that the resonance frequency of the geometrically restricted partner spin lies within the pump band. In contrast, a broadened observer frequency range selects more of the randomly oriented spins in the sample to participate in the experiment which in turn should increase sensitivity. However, a broader observer frequency range only increases the probability of the partner spin to resonate at the pump frequency, if the constrained geometry requires a specific frequency offset, which was not excited before with narrowband (monochromatic) observation. A broadened observer frequency range therefore often does not have a significant influence on λ, as we find it here when comparing the S_oM_p and M_oM_p setup.

A further increase in modulation depth λ to 35% was observed for the combination of shaped observer pulses with a shaped pump pulse (S_oS_p). We tentatively explain this increase in λ to orientation selection for this geometrically correlated bis[Cu(II)-PyMTA] ruler: the additional spins that are excited by the broadened observer frequency range in comparison to the monochromatic observer pulse select a set of molecular orientations that due to the geometrical constraint have a higher probability that their partner spin is resonant with the pump frequency band.

The dipolar spectra shown in Fig. 6(c) provide no arguments in favour of or against this hypothesis. Dipolar spectra detected with the M_oS_p and S_oS_p setups are very similar, i.e. the set of detected orientations of the spin-spin vector with respect to the external magnetic field B_0 are similar. However, it would still be possible that the probability of the observed spin to be the partner spin of one of the pumped spin packets is increased by the S_oS_p setup, which would then result in the higher λ. Furthermore, the dipolar spectra for the setups with shaped pump pulse closely resemble a superposition of Pake patterns. This suggests that a larger subspace of θ values is sampled by the shaped pulses applied here. In contrast, the M_oM_p and the S_oM_p dipolar spectra both do not resemble a superposition of Pake patterns. The subspace of sampled θ values is thus clearly not sufficient for detection of the complete Pake pattern. A comparison of the distance distributions computed with neglect of orienation selection is presented in Fig. SI 11.

Unexpectedly, with shaped observer pulses the observed noise level $n_{l,M}$ was slightly higher than for the otherwise equivalent setup with monochromatic observer pulses in Fig. 6(a). This observation was made with monochromatic (M_p) as well as with shaped pump pulses (S_p). A yet larger increase in $n_{l,M}$ was observed in S_oS_p with respect to M_oS_p DEER measurements for a setup, in which the observer bandwidth was placed around B_{max} with Δf_{obs} set to 0.5 GHz, as optimized for sensitivity in Section 3.2.2. Here, Δf_{pump} was 1.2 GHz, the data are shown in Fig. SI 7. Much higher noise levels were also found for S_o than M_o DEER measurements with the same setup as in Fig. 6 but with the observer and pump band inverted, i.e. the observer band covering B_{max} and the pump band the spectral region towards the low-field shoulder, see Fig. SI 8. All noise levels are provided in Table SI 5. It thus appears as if the increase in noise level was more pronounced if the observer pulses were placed around the maximum of the Cu(II)-PyMTA spectrum compared to placing the observer pulses towards the low-field shoulder. As discussed above in Section 3.2.2, the increase in detectable coherence saturates for $\Delta f > 0.5$ GHz if shaped observer pulses are placed around B_{max} and no pump pulse is applied. We currently do not understand why shaped observer pulses lead to increased noise levels in dipolar data despite the fact that more spins are observed in the experiment. A thorough understanding of this observation requires a dedicated study.

Note that in some cases we also observed higher noise levels $n_{l,M}$ in the DEER trace when the pump pulse was shaped instead of a monochromatic pulse, see Fig. 6(a). This increase in noise $n_{l,M}$ was observed in the form factor in time domain, however, in some cases it was masked in the noise evaluation $n_{l,FT}$ from dipolar spectra by the improved modulation depth, see Table SI 5 in the SI. The increase in noise $n_{l,M}$ for shaped pump pulses was large in the measurements where the observer was far from the spectral maximum in Fig. 6(a), however it was not significant when the observer pulse was positioned on the spectral maximum, see Fig. 5(a). We tentatively explain this increase in noise level $n_{l,M}$ by off-

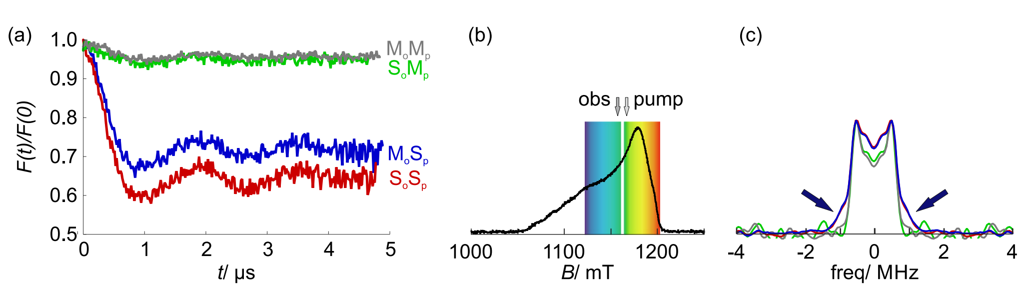

Fig. 6. DEER with monochromatic (M) and shaped (S) observer ($_o$) and pump pulses ($_p$) at Q band: M_oM_p (grey), S_oM_p (green), M_oS_p (blue), S_oS_p (red). (a) DEER background-corrected form factors, (b) echo-detected field sweep with pulse ranges indicated by colored boxes, (c) dipolar spectra. A strong increase in modulation depth λ and recovery of the shoulders of the dipolar spectrum is observed upon shaping the pump pulse. (For interpretation of the references to colour in this figure legend, the reader is referred to the web version of this article.)

resonant Bloch-Siegert phase shifts ϕ_{BS} caused by the individual pumped spin packets on the observer spin packets. Due to the disparity in ϕ_{BS} for different offsets, destructive interference results in echo reduction. Such phase shifts have been observed before in Gd(III)–Gd(III) UWB DEER and were alleviated there by application of two pump pulses, one on either side of the observer frequency [99]. This effect is expected to be amplified if the observer pulses are shaped: ϕ_{BS} now depends on the offset of each specific observer spin packet to its respective pumped spin packet.

To conclude our findings for DEER experiments with shaped pulses, we found very large improvements in sensitivity when substituting the monochromatic pump pulse by a shaped one in DEER experiments with monochromatic observer pulses. This effect was especially strong in X band, where nearly the whole spectrum can be included in the experiment. Combining shaped observer pulses with a shaped pump pulse did result in an increase in nominal modulation depth over the equivalent experiment with monochromatic observer pulses. We attribute this otherwise unexpected finding to orientation selection effects. Shaped observer pulses lead to an increase in noise level that is contradicting the increase in peak intensity in the echo transients. Sweeping only the observer pulses did not increase the modulation depth significantly. This is in agreement with expectations as the modulation depth in DEER corresponds to the fraction of B spins that are pumped for the observer-selected molecular orientations. A broader observer band thus detects more molecular orientations (as A spins), but might not necessarily increase the probability that the coupled spin resonates within the pump band. Dipolar spectra resembling a superposition of Pake patterns were detected in the measurements using shaped pump pulses provided Δf_{pump} covered a significant part of the spectrum. This suggests that orientation selection was largely suppressed. In the following, we will explore the sensitivity of RIDME experiments with monochromatic as well as shaped observer pulses before we discuss orientation selection in DEER and RIDME in detail in Section 3.5.

3.4. RIDME experiments

3.4.1. Rectangular pulses

In contrast to the DEER experiment, where inversion of the B spins is achieved by applying a pump pulse at a second frequency band, in RIDME B spins are inverted by stochastic longitudinal relaxation events and thus a single frequency band is sufficient. This poses lower technical requirements to (i) the spectrometer and (ii) the resonator. Further, the observer frequency can be placed freely in the resonator and in the EPR spectrum of the A spins, so that the position of highest sensitivity can be chosen. This implies that the performance of the RIDME technique is drastically improved in resonators with a higher quality factor *Q*, which induce a higher signal intensity at the same spin concentration (see Table SI 4 and SI 5 for a comparison of the loop-gap and TE_{102} box resonator).

The modulation depth is determined by the time allowed for longitudinal spin flips during the mixing block and builds up according to the probability P_{odd} of an odd number of spin flips during the mixing block:[118]

$$P_{odd} = \frac{1}{2}\left[1 - \exp\left(-\frac{T_{mix}}{T_{1,B}}\right)\right]. \tag{6}$$

Note that this equation uses the assumption that longitudinal relaxation of paramagnetic centres in frozen glasses is monoexponential as well as that it neglects correlated flip-flops of the A-B pairs. The latter effect can cause a reduction of the limiting value for the maximal achievable modulation depth.

As in the DEER experiment, an initial preparation period creates electron coherence, which is in RIDME subsequently stored in the direction of the external static magnetic field in form of a polarization grating. This results in a loss of half of the originally excited magnetization. After the mixing time, the magnetization is transferred back into the transverse plane, where it is eventually detected after refocusing by another π-pulse.

By adjusting the length of the mixing interval T_{mix} several parameters can be tuned. A long mixing time leads to a higher probability of B-spin flips and thus efficient spin inversion, which in turn results in a large modulation depth. However, also some A spins will loose their phase information by longitudinal spin flips and thus the signal intensity is reduced. Further, a longer mixing block allows for more efficient spectral diffusion in that time and thus the background decay is accelerated [77, 82].

These findings are presented for a set of mixing times in Fig. 7(a and b). Fig. 7(b and c) further shows that the shapes of the RIDME form factors in time domain as well as in frequency domain for different mixing times remain largely constant apart from some zero-frequency components which we attribute to imperfect background correction. The consistency in form factor shape for different mixing times supports the assumption, that no orientation selection due to different relaxation of the various spin packets is introduced to the Cu(II)-Cu(II) dipolar evolution data – at least for this very sample over the studied range.

A fast and simple experiment to probe the optimal length of the mixing block is depicted in Fig. 8. It is based on a similar idea as the two-point optimization for the DEER pump pulse parameters shown in Fig. 4. Two points of a RIDME trace are measured while the mixing time is varied: the zero time point, representing the maximum signal intensity $S(t = 0)$ (Fig. 8(a)) and a later time point before the minimum of the first oscillation, e.g. 500 ns after the zero time point $S(t)$ indicated by the grey, dashed line in Fig. 7 (b). The intensity difference between the two time points can serve as an estimate λ_{2P} of the modulation depth (Fig. 8(b)) and, if well chosen, can reproduce the measured modulation depth for a full RIDME trace (see dark blue diamonds in Fig. 8(b)). Note that the steep background decay can cause deviations between λ_{2P} and the true modulation depth. The product of signal intensity and modulation depth serves as estimate for the sensitivity $\eta_{2P} = S(0) \cdot \lambda_{2P}$ of the experiment.

Fig. 8(c) shows that there is a range of mixing times with best sensitivity, resulting from the trade-off between best signal intensity and highest modulation depth. The trends resulting from this estimate are in qualitative agreement with sensitivity measures from full RIDME traces, that also take noise into account (purple circles, see Table SI 4). Note that the two-point optimization underestimates noise contributions at the end of long time traces as noise is not equally distributed over the background-corrected RIDME form factor. Noise strongly increases towards the end of the dipolar evolution time due to the shape of the background function. For long time traces, in which the signal decays significantly due to the background contribution for long mixing times, it is thus advisable to use a T_{mix} towards the beginning of the 'optimal range'. A shorter T_{mix} is also preferable for conditions with very strong background curvature, i.e. in protonated solvent. For short time traces, however, the signal at the end of the dipolar trace is not yet decayed significantly due to the background contribution and thus a long T_{mix} can be chosen to exploit the larger modulation depth.

For the bis[Cu(II)-PyMTA] ruler presented here, highest sensitivity is achieved at a mixing time of approximately $T_{mix} \sim 3/4 \cdot T_1$ with a modulation depth of about 30%. A maximal modulation depth of almost 50% can be achieved at the cost of signal intensity and faster background decay for longer T_{mix}.

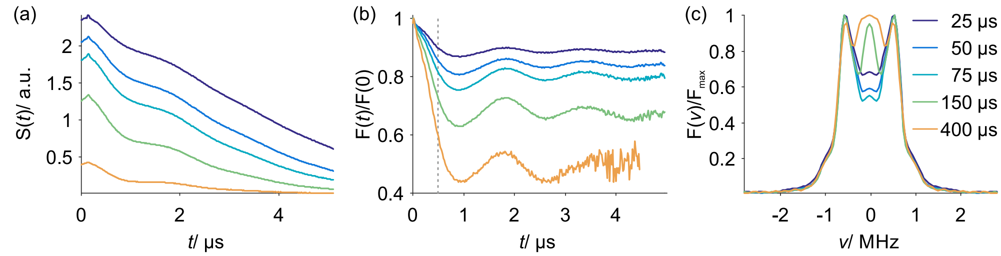

Fig. 7. Dependence of RIDME traces on mixing time in Q band and at 20 K. (a) Primary data, (b) background-corrected form factors in time and (c) frequency domain. The different mixing times are colour coded. The grey dashed line in (b) corresponds to the second time point used in the two-point optimization in Fig. 8. (For interpretation of the references to colour in this figure legend, the reader is referred to the web version of this article.)

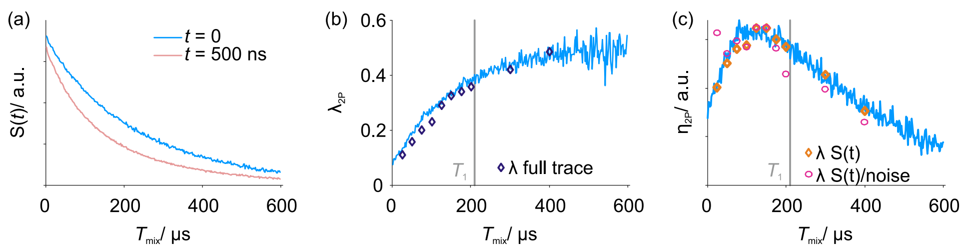

Fig. 8. Two-point optimization curves for RIDME experiments. (a) Signal intensity for $t = 0$ (blue) and $t = 500$ ns (rose). (b) Estimate of modulation depth λ_{2P} based on difference of signal intensity at $t = 0$ and $t = 500$ ns (blue). Dark blue diamonds give the modulation depth λ extracted from full RIDME traces. (c) Sensitivity estimate η_{2P} from product of signal intensity at $t = 0$ and modulation depth estimate λ_{2P} (blue), the same product for full RIDME traces (orange diamonds) and a sensitivity estimate taking noise into account (purple). The grey vertical lines mark the longitudinal relaxation time T_1 extracted from fitting $c \cdot \exp(-t/T_1)^x$ to the inversion recovery experiment at the same measurement temperature and detection position. (For interpretation of the references to colour in this figure legend, the reader is referred to the web version of this article.)

Non-negligible contributions of A-spin flips induced by B-spin flips may cause some reduction in modulation depth. Note that echo-crossings around the zero-time [81] may slightly overestimate the modulation depth presented here. A similar effect was observed in a study of nitroxide-Cu(II) rulers in our lab [102].

Depending on the interplay of background decay and trace length required to access the distance of interest, the maximal mixing time may be restricted. In addition to the DEER background decay from intermolecular interactions, contributions from spectral diffusion arise during the mixing block in the RIDME experiment. With increasing mixing block duration these effects become more pronounced and the background decay is accelerated. A comparison of the background decay for the DEER and the RIDME experiment is shown in the Supporting Information, Fig. SI 9. The efficiency of the electron-nuclear spectral diffusion process depends on the surrounding nuclei and thus on the solvent, e.g. the effect will be more pronounced in proton-rich than in deuterated environments [82]. Thus, the choice of the solvent is not only an important parameter in terms of transverse evolution time, but also for the curvature of the RIDME background decay. On the other hand, for short distances and consequently short time traces, loss in signal intensity and faster background decay are less significant, so that longer mixing times may be used to increase the modulation depth.

To summarize, we observed an increase of the modulation depth accompanied by a decrease in signal intensity with increasing T_{mix} in RIDME measurements. A two-point optimization was found to provide a good basis to choose T_{mix} with respect to sensitivity. The choice of T_{mix} further depends on the distance of interest as the background decay is accelerated at longer mixing times. This effect is expected to be particularly strong in protonated environment.

3.4.2. RIDME with shaped pulses

We explored the use of shaped pulses in RIDME measurements. Optimization of the shaped observer pulses for RIDME is simpler than in DEER for two reasons: (i) in contrast to DEER, only one frequency band is necessary for excitation in RIDME. The shaped observer pulses could therefore be placed symmetrically in the centre of the resonator. (ii) The observer pulses can be placed freely in the spectrum, as the excitation bandwidth for the B spin is not limited by excitation in the RIDME experiment.

The shaped observer pulses were sweeping a frequency range which was placed symmetrically around the maximum of the Cu(II)-PyMTA spectrum. This choice was motivated by highest signal intensity as well as by the fact that most orientations of the spin-spin vector contribute in this region, which should reduce orientation selection [73].

We compared RIDME traces recorded with monochromatic pulses to RIDME traces acquired with HS6 pulses of bandwidth Δf = 0.5 GHz. This bandwidth was found to provide optimal sensitivity for two-pulse echoes of shaped pulses in Section 3.2.2. Despite the larger excitation band of the shaped pulses, we observed a reduction in SNR in the RIDME traces with shaped pulses compared to using monochromatic pulses in the same broadband (loop-gap) resonator (data not shown). The sensitivity values are provided in Table SI 5: at the same mixing time of 50 μs, RIDME using shaped pulses exhibits with $4 \cdot 10^2$ significantly lower sensitivity than RIDME using monochromatic pulses ($1.3 \cdot 10^3$) in the same resonator. The higher noise levels found in DEER measurements with the same shaped observer pulses are thus reproduced in the lower SNR of RIDME experiments with these pulses. If monochromatic pulses are used in a resonator with narrower bandwidth and larger sample volume, the sensitivity is further increased to $2.4 \cdot 10^3$. As RIDME does not utilize a broadband pump pulse, the use of a resonator with higher Q increases the detection efficiency while restricting only the bandwidth of the observer band. In summary, shaped observer pulses required the use of a broadband resonator, yet yielded lower sensitivity than measurements with monochromatic pulses in the same resonator. For RIDME experiments with monochromatic pulses, a resonator with higher Q, and thus higher detection sensitivity, is more beneficial.

In order to compare form factors of RIDME traces acquired with monochromatic or shaped pulses with high SNR, in Fig. 9 we show traces that were recorded with different numbers of scans. The shape of the RIDME form factors detected by pulses covering 0.5 GHz slightly changes compared to the form factors obtained with monochromatic pulses with pulse bandwidth $\Delta f \approx 40$ MHz. Both types of pulses were positioned symmetrically at and around the maximum of the Cu(II)-PyMTA spectrum, respectively. The dipolar spectra detected by RIDME recorded with shaped as well as with monochromatic pulses show deviations for higher dipolar frequencies, i.e. the contributions corresponding to $\theta = 0^{\circ}$. In the time domain this translates to slight deviations in the form factor shape for early dipolar evolution times. This indicates an influence of orientation selection, which will be discussed in Section 3.5. For now we note that the weighting of this frequency contribution is yet different for field-averaged RIDME data, but no additional frequencies occur. This finding corroborates the assumption that both perpendicular and parallel orientations of the spin-spin vector with respect to the external field contribute at this detection position.

The RIDME background decay does not significantly vary with the pulse bandwidth (see Supporting Information, Fig. SI 9). This suggests that instantaneous diffusion due to the microwave pulses negligibly contributes to the RIDME background decay in deuterated frozen glassy matrices at the concentration used here and that for these conditions the RIDME background shape is dominated by spectral diffusion during the mixing block.

To conclude, we found a similar reduction in SNR when using shaped compared to monochromatic observer pulses in the RIDME experiment and in the DEER experiment. The shape of the RIDME form factor and thus the dipolar spectrum were only slightly affected by the change from monochromatic to shaped observer pulses with larger bandwidth for detection at the maximum of the Cu(II)-PyMTA spectrum.

3.5. Orientation selection in DEER and RIDME

The spectral width of the Cu(II)-PyMTA EPR spectrum in Q band does not allow for its full excitation even on a spectrometer with high-power microwave output and broadband pulse shaping capabilities. This leads to the afore-mentioned orientation selection effects [52].

In Section 3.4.1, it was shown that the RIDME form factors are largely constant over a wide range of mixing times from $0.1T_1$ to $2T_1$. We thus assume that the probability of longitudinal relaxation is approximately equal across the full spectrum and orientation selection from the inverted spin can be neglected, even though longitudinal relaxation times vary across the spectrum (see Fig. SI 2 in the SI). Thus, in the case of the RIDME experiments only orientation selection from the observer spin contributes which restricts the dipolar angle θ if the system has a fixed geometry. The latter effect needs to be studied for a set of different detection positions across the Cu(II)-PyMTA spectrum.

In contrast, the detected subspace of θ is further limited in the DEER experiment by the restriction that the frequency of the coupled (pumped) spin for the observer-selected geometry has to be contained in the pump-pulse excitation band. In Figs. 5 and 6, we observed changes in the dipolar spectra with the bandwidth Δf of the pump pulse in UWB DEER.

In the following we investigate how the restriction of the detected dipolar angles θ by an UWB pump pulse ($\Delta f_{pump} = 0.8$ GHz) in DEER compares to a B-spin flip by inversion in RIDME experiments for the stiff bis[Cu(II)-PyMTA] ruler with correlated g-tensor orientations of the Cu(II) centres at several field positions. In both experiments, the observer pulses were monochromatic and the field position is indicated with respect to the observer frequency. For the DEER experiments, two data sets were acquired: one, in which the pump band was positioned below the observer frequency ($\nu_{pump} < \nu_{obs}$), and the other one with the opposite arrangement $\nu_{obs} < \nu_{pump}$. The sum of the two traces with same ν_{obs} were compared to the RIDME traces as well as the individual data sets. This is illustrated in Fig. 11(a–d) for detection at the maximum of the Cu(II) spectrum. The full comparison of DEER and RIDME traces at all fields is shown in Fig. SI 13. The different detection positions and DEER setups are illustrated in Fig. SI 12. Note that in the evaluation of the data presented here, the g-value of the free electron g_e was used.

Fig. 10 shows the dipolar spectra for detection at (a) the maximum and (b, c) in the low- and high-field regions of the spectrum. For both techniques, the dominant dipolar frequency changes from 0.6 MHz for observation at fields $\leqslant B_{max}$ (Fig. 10(a andb)) to 1.2 MHz at higher fields than B_{max} (Fig. 10(c)). The strongest differences between the summed DEER trace and RIDME are observed in regions in which mainly x/y-orientations of the g- and A-tensors contribute, e.g. at B_{max} and at higher fields as shown in Fig. 10(a and c). For these field positions, the DEER traces are sensitive to the position of the pump pulse: either the perpendicular or the parallel contribution to the dipolar signal is enhanced as demonstrated for detection at B_{max} in Fig. 11(a–d). At lower fields, the dipolar spectra from RIDME and the different DEER setups largely agree.

Averaging over a full set of RIDME as well as DEER data does result in the same distance information. The summed dipolar data are shown in Fig. 11(e–h). This suggests that with the applied averaging scheme most of the dipolar frequencies are detected. However, fitting such data with DeerAnalysis which assumes a superposition of Pake patterns in frequency domain reveals slight deviations between the experimental data and the fit around $\theta = 0^{\circ}$ (arrows in Fig. 11(g)) indicating residual orientation selection. We observed similar effects for bisnitroxides in Q band, which will be discussed elsewhere.

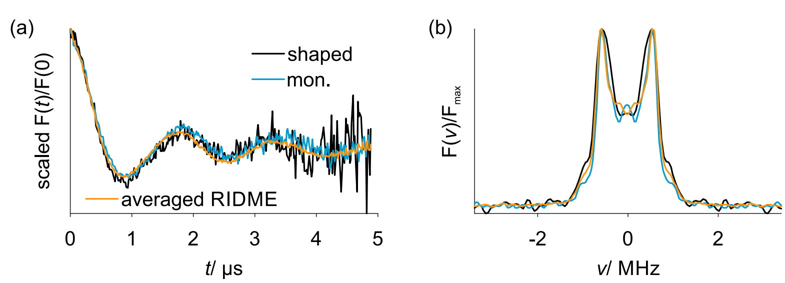

Fig. 9. Comparison of Q-band RIDME data for shaped (black) and monochromatic pulses (blue) at 20 K recorded using the broadband resonator, $T_{mix} = 75$ µs. Data from field averaged RIDME measurements detected in a resonator with higher Q are overlaid in orange ($T_{mix} = 30$ µs). (a) Scaled form factors in time domain F(t) and (b) dipolar spectrum F(ν). (For interpretation of the references to colour in this figure legend, the reader is referred to the web version of this article.)

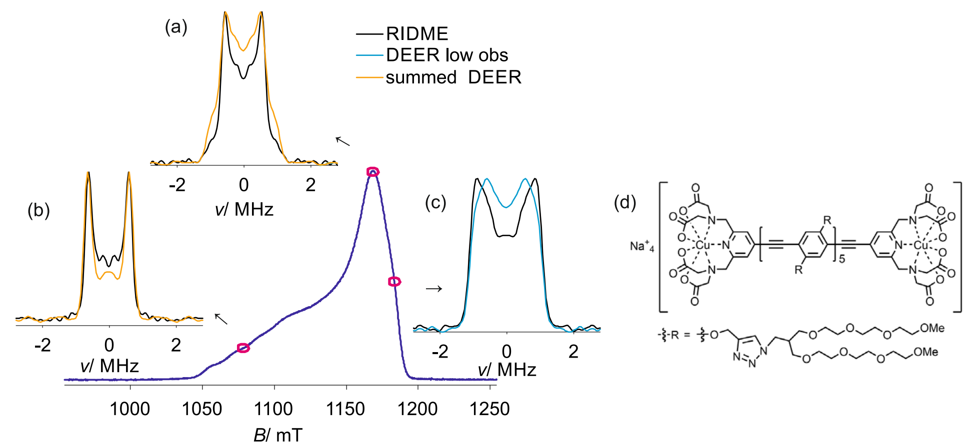

Fig. 10. Comparison of Q-band DEER (coloured) and RIDME (black) normalized dipolar spectra at different field positions indicated on the Cu(II)-PyMTA spectrum (purple). (a) Detected at B_{max}, (b) $B_{max} - 90$ mT and (c) $B_{max} + 15$ mT. (a and b) DEER traces obtained by summing over two setups (yellow) with $\nu_{obs} < \nu_{pump}$ and $\nu_{pump} < \nu_{obs}$ and (c) $\nu_{obs} < \nu_{pump}$ (low obs, blue). (d) Structure of the bis[Cu(II)-PyMTA] ruler. (For interpretation of the references to colour in this figure legend, the reader is referred to the web version of this article.)

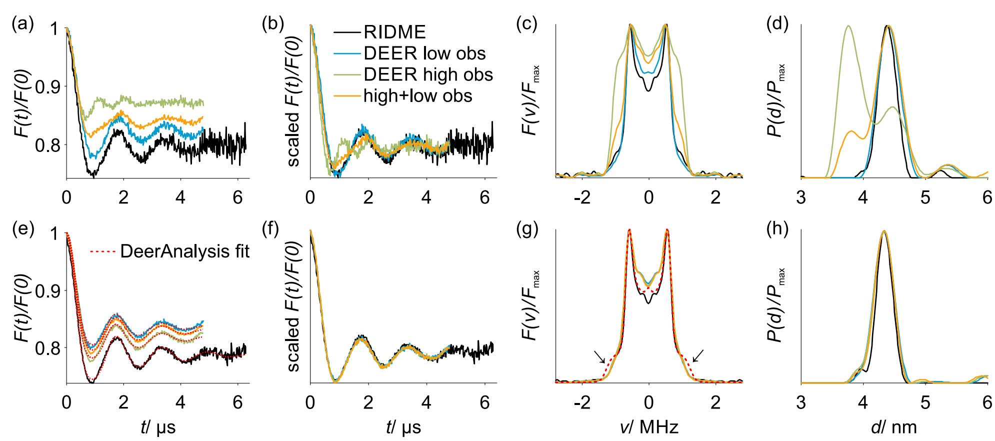

Fig. 11. Comparison of Q-band DEER (coloured lines) recorded with different relative positions of the pump pulse with respect to the observer and RIDME (black). (a–d) Detected at maximum field B_{max} and (e and f) field averaged. DEER setups were recorded with $\nu_{obs} < \nu_{pump}$ (low obs, blue) and $\nu_{pump} < \nu_{obs}$ (high obs, green). (a and e) Form factors in time domain, (b and f) modulation-depth scaled form factors in time domain, (c and g) dipolar spectrum, (d and h) apparent distance distributions. In (e) and (g) fits resulting from DeerAnalysis are overlaid as red dashed lines. The arrows in (g) indicate frequencies for which deviations between the dipolar spectra and the fit are observed. (For interpretation of the references to colour in this figure legend, the reader is referred to the web version of this article.)

Furthermore, for the system studied here and detection at B_{max} – where both parallel and perpendicular orientations contribute – the RIDME experiment as well as the DEER experiment with $\nu_{obs} < \nu_{pump}$ already closely resemble an average over the full Cu(II)-PyMTA spectrum and the resulting changes in the apparent distance distributions are small, but noticeable, see Fig. SI 11(d–f).

The g-tensor can be extracted from lineshape analysis as described in the Supporting Information. It allows us to calculate an effective g-value as an average over all orientations according to Eq. (3) and averaging over the full angular space. For Cu(II)-PyMTA, an effective g_{eff}-value of 2.131 is obtained. This already deviates significantly from the g-value of the free electron, which is typically assumed for distance analysis.

Fig. 12 shows the influence of the g-value on the apparent distance distribution. Two different situations are compared: the use of the g-value of the free electron ($g_e = 2.0023$) as implemented in DeerAnalysis and the effective g_{eff}-value to compute the dipolar coupling constant w_{dd} (Eq. (2)). The difference in g-values leads to a shift of ~2 Å in the extracted Cu(II)–Cu(II) mean distance: from 4.3 to 4.5 nm.

The distance of ~4.5 nm is much closer to the distance of ~4.7 nm measured for the same molecular rulers with Gd(III) [100,107,119] or Mn(II) [114] as metal centres. A small shift towards shorter distances is not astonishing in the case of the bis[Cu(II)-PyMTA] ruler due to the smaller ionic radius of Cu(II) [120], although this effect is expected to be smaller than 0.2 nm. Further, the Cu(II) ion is most probably more strongly coordinated by the three nitrogen atoms and thus is expected to sit closer to the pyridine ring. In addition, the shorter distance might also indicate a higher spin density at the coordinating nitrogen atoms for Cu(II)-PyMTA as compared to Gd(III)-PyMTA and Mn(II)-PyMTA.

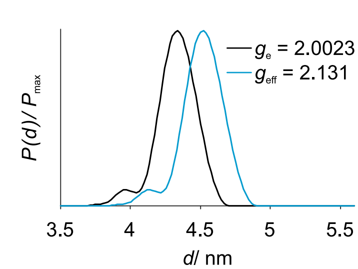

Fig. 12. Influence of g-value on distance distribution for the field-averaged RIDME data in Q band, 20 K, $T_{mix} = 30$ μs.

Nevertheless, the distance of 4.5 nm is much more likely to be correct than the one of 4.3 nm. We thus conclude that g-values should be adjusted in distance analysis routines of spin tags with significant deviation of g_{eff} from g_e.

Note that using the effective g-values as computed from Eq. (3) and averaging over the full angular space is an approximation. In principle, the true g-value average also depends on the relative orientation of both spins and is given as $\langle g_A \cdot g_B \rangle$, while in our approach we assumed no correlation, i.e. $\langle g_A \cdot g_B \rangle = \langle g_A \rangle \cdot \langle g_B \rangle$, and ignored the angular dependencies of both g-values. The influence of the correlation and angular dependencies is expected to be much smaller than the shift between g_e and g_{eff}, but it might cause complications in quantitative analysis of orientation selection. Note further that the effective g-value is calculated in the spin Hamiltonian after the Bleaney transformation, which tilts the magnetic field experienced by the spin with respect to the direction of the static magnetic field. Thus, also the quantization axes of the $\widehat{S}_z$ operators in Eq. (1) do no longer coincide with the direction of the static magnetic field. However, this is expected to cause only a weak perturbation in the case of about 10% g-anisotropy presented here. The problem can become relevant for spin systems with yet larger g-anisotropy.

Eventually, Fig. 11 reveals that excitation of dominantly perpendicular orientations of the axial g-/A-tensors favour a parallel orientation of the inter-spin vector with respect to the external magnetic field ($\theta = 0^\circ$). In contrast, excitation of the z-orientation of the Cu(II)-PyMTA spectrum correlates to the perpendicular orientation ($\theta = 90^\circ$). This indicates that the parallel orientations of the g-/A-tensor are along the long axis of the molecular ruler and the perpendicular tensor orientations are along the short axis of the molecular ruler.

3.6. Advantages and disadvantages of DEER and RIDME

The sensitivity of the two experiments is influenced by many factors, which can have converse effects in DEER and RIDME. These factors include the microwave frequency band, the available pulse power and shapes, the resonator bandwidth and B_1 as well as intrinsic sample properties such as the distance of interest or the spin center environment, e.g. the degree of solvent protonation.

We found that similar sensitivity can be achieved by the two techniques if the experimental conditions are optimized for each method (see Table SI 4 and 5 in the Supporting Information). For example, at the commercial Bruker Elexsys E580 spectrometer (Table SI 4) it was possible to reach a sensitivity value η of $2.5 \cdot 10^4$ in RIDME using a TE_{102} resonator for 3 mm samples [110] while the use of a loop-gap resonator [105] at the same spectrometer allowed to reach an UWB DEER sensitivity of $2.4 \cdot 10^4$ by application of a shaped pump pulse. At our home-built broadband spectrometer (Table SI 5), the sensitivity η of DEER with an UWB pump pulse even surpassed the sensitivity of RIDME in either resonator by about a factor of 2.

That it is possible to reach similar or higher sensitivity by UWB DEER as with RIDME demonstrates the sensitivity advantage by UWB pulses: when only monochromatic pulses are used, the sensitivity comparison will favour RIDME. For example, a study which was published during the reviewing process of this work [121] found a 100 times higher sensitivity for Q-band RIDME in a critically coupled 3 mm resonator compared to monochromatic-pulse DEER under overcoupling conditions. As mentioned above, such a comparison strongly depends on the choice of resonator bandwidth and spectrometer. Using the same resonator with the same coupling conditions and the same, commercial spectrometer for both experiments, we found the sensitivity η of RIDME to be 2–3 times higher than the one of DEER with monochromatic pulses: $1.2 \cdot 10^4$ compared to $5 \cdot 10^3$ in the loop-gap resonator and $2.5 \cdot 10^4$ compared to $1.2 \cdot 10^4$ in the TE_{102} resonator (Table SI 4).

Before we discuss the relative performance of the two techniques under a variety of experimental conditions, in the following we briefly summarize our findings regarding individual optimization of the two pulse sequences.

For UWB DEER, we found a large increase in modulation depth λ and thus sensitivity by the use of a shaped pump pulse. Due to the narrower spectrum, the gain was particularly large in X band where $\lambda = 44\%$ was feasible in the commercial MS3 resonator combined with a TWT with nominally 1 kW output power. The gain in sensitivity for UWB DEER depends on the shortest distance $r_{\min}$ due to the limitation of the pump pulse length t_p by $t_p < \frac{T_{dd}}{4}$. In our case this translated to a λ of 24% compared to 36% for $r_{\min} > 2.75$ nm and 3.7 nm in Q band, respectively. On the other hand, in RIDME measurements a trade-off between modulation depth λ and signal intensity was observed with increased length of the mixing block T_{mix}. Furthermore, the choice of T_{mix} depends on the background decay. For the compound studied here a maximal λ of nearly 50% was observed, while the λ for best sensitivity was found in the order of 30%.

UWB DEER benefits from high resonator bandwidth and B_1, while this is not beneficial for the RIDME technique. If only a resonator with higher Q and low bandwidth is available, the gain in modulation depth in UWB DEER is smaller. Spectrometers with low microwave power (and thus low B_1) and high sensitivity-detection with small bandwidth, accompanied by a resonator with higher Q, yield favorable results for the RIDME experiment with monochromatic pulses. Note also the simplified setup in comparison to UWB DEER and that a single frequency source is sufficient.

However, the requirements of high power and high bandwidth are reintroduced for RIDME in combination with shaped observer pulses. Yet, shaped observer pulses in Q band did not introduce any additional dipolar frequencies for detection in the region of $B_{\max}$. Instead, the SNR of DEER and RIDME traces with shaped observer pulses around $B_{\max}$ was decreased even though the peak echo intensity was found to be increased for broader observer pulse bandwith Δf_{obs}. This matter appears to deserve a dedicated study. Thus, we currently conclude that frequency-swept observer pulses seem not to be beneficial in terms of higher sensitivity. However, they appear more promising for experiments in which a good separation between different microwave frequency bands is necessary [97,98,122] or in which the full spectrum can be excited. This enables correlation of EPR and dipolar spectra [109] or simplifies orientation averaging [102]. Note that for the bis[Cu(II)-PyMTA] ruler studied here, it is impossible to excite the full EPR spectrum with a single broadband pulse with the given EPR setup in Q band.

For the bis[Cu(II)-PyMTA] compound studied here, a ruler with a very stiff spacer, the same dipolar spectrum was attained by field averaging of UWB DEER and RIDME traces. Detection at individual field positions revealed differences between DEER and RIDME for $B \geqslant B_{\max}$ as well as for different positioning of the pump band relative to the observer band in DEER. These observations are in line with partial excitation of orientations. Selective excitation by the pump band might be an advantage and a disadvantage of UWB DEER at the same time: while it maintains the possibility for orientation selection studies it needs to be taken into account for accurate distance determination in very stiff systems. In contrast to UWB DEER, orientation selection in RIDME was solely dominated by the observer pulses. Thus, RIDME data might be easier to interpret for systems with highly correlated geometry. Finally, the quality of RIDME data is expected to remain the same independent of the width of the B-spin spectrum and spectral separation, i.e. for systems with broader spectra or different spin labels with well-separated EPR spectra [75,79,102,123,124].

Electron Spin Echo Envelope Modulation (ESEEM) introduces hyperfine frequencies to the dipolar evolution data due to coupling of the electron spin to nearby nuclei that interfere with the distance analysis. These effects are less important at high frequencies (W band and above), since at those conditions the nuclear Zeeman interaction is typically much larger than the hyperfine coupling, which suppresses ESEEM contributions. Due to the nature of the pulse sequence, these effects are more pronounced in the RIDME experiment [77,111,123] and might hinder application of the RIDME technique at low frequencies. For instance, deuterium ESEEM is often pronounced in X band and complete suppression of nuclear modulations in RIDME was found to be difficult (data not shown). UWB DEER therefore appears advantageous over RIDME for measurements at lower frequencies, in particular in X band. In X band, the sensitivity of UWB DEER was even found to be similar to Q-band DEER on our home-built spectrometer. On the other hand, the RIDME technique may be beneficial at high frequencies where EPR spectra of some spin labels become very broad while broadband resonators and high microwave power outputs are currently less common and more difficult to construct.

Lastly, the steeper background decay in RIDME experiments may restrict the distance range and complicate data analysis, especially for long distances. This problem is notably enhanced in protonated solvents for which spectral diffusion is much more efficient [82]. On the other hand, at both X- and Q-band frequencies, the quality of the UWB DEER data was increased with increasing $r_{\min}$ due to the possibility to use a longer pump pulse. It follows that UWB DEER may be advantageous for the detection of long dipolar evolution times, i.e. long spin-spin distances, and RIDME for shorter spin-spin distances.

To summarize, the choice of technique depends on the following factors:

(i.) The spectrometer: In X band, UWB DEER performs well whereas RIDME measurements would be more difficult due to nuclear modulation effects. Low amplifier power, i.e. low B_1, would hinder application of UWB DEER. Broadband experiments may impose strict requirements on spectral purity of the excitation, for instance on sufficient suppression of the local oscillator frequency. The RIDME setup neither requires high spectrometer bandwidth nor a second frequency source.

(ii.) The resonator: Resonators with higher Q and with low bandwidth Δf_{res} improve the sensitivity of RIDME experiments while the lower average B_1 limits the modulation depth in UWB DEER. The opposite is true for resonators that can be operated at low Q like the X-band MS3 resonator or Q-band loop-gap resonators [105,106,125].

(iii.) The distance of interest: For long dipolar evolution times, the RIDME signal might be already significantly decayed due to background contributions. Thus, background correction of the RIDME data can strongly enhance the noise level towards the end of the time trace. At the same time, the sensitivity of UWB DEER is limited by the shortest distance $r_{\min}$ which in turn limits the pump pulse length. The sensitivity in UWB DEER increases with increasing $r_{\min}$ for the same length of DEER traces. The longest distance of interest is limited by the detectable trace length, which depends on the phase memory time. In RIDME, the signal might be potentially decayed to zero due to the background decay already before the phase memory limit is reached.

(iv.) The sample geometry: Albeit the same dipolar spectrum was obtained from field-averaged RIDME and UWB DEER for the sample studied here, this might not be a general result. Orientation selection might be more difficult to average by UWB DEER in some other samples, whereas it may also be less critical for Cu(II)-based labels attached to a protein by a more flexible linker than observed here for a stiff Cu(II)–Cu(II) ruler. In cases where information on the relative orientation is sought, RIDME can not deliver this information unless the relaxation is strongly anisotropic.

(v.) The solvent: A higher degree of deuteration generally prolongs the decay of observable coherence both in DEER and RIDME. In case of the RIDME technique, solvent deuteration also strongly reduces the contribution of electron-nuclear spectral diffusion to the RIDME background decay, i.e. the curvature of the background. However, depending on the microwave frequency and the strength of forbidden transitions, deuteration might introduce nuclear modulations which might be more difficult to average for RIDME, especially at X-band frequencies. For protonated environments, the DEER background decay is less curved and can therefore be fitted more reliably.

(vi.) The combination of spin labels: Large spectral separation in systems with two different spin labels might hinder applicability of UWB DEER while performance of RIDME is expected to be unaffected.

4. Conclusions

We compared RIDME and DEER experiments for the measurement of dipolar couplings in a bis[Cu(II)-PyMTA] ruler and investigated the use of shaped pulses in both pulse sequences. The two techniques require different optimization of instrumental parameters, as for example the resonator bandwidth. Furthermore, their relative performance varies with the spectrometer band and the sample requirements. We found both methods to provide high-quality data with good and similar sensitivity if the experimental setup was adjusted for the respective sequence. From our findings it becomes apparent that there is not one best method, but that the optimal choice depends on the system under investigation.

Application of a shaped pulse to substitute the monochromatic pump pulse of the DEER sequence led to large gains in modulation depth and correspondingly in sensitivity in X and Q band. At X-band frequencies and with a commercial MS3 resonator, it was possible to include nearly the whole spectrum in the experiment. These are very promising results, especially with respect to the ongoing development of Cu(II)-based spin labels which are often anchored with little conformational flexibility. For such systems, distance determination with good sensitivity and without orientation selection presents a challenge, which X-band DEER with a shaped pump pulse might help to address in the future.

Orientation selection in RIDME was found to be independent of the mixing time. A trade-off between signal intensity and modulation depth was found depending on the measurement parameters. A simple two-point optimization experiment provides a good estimate for finding the mixing time which yields the highest sensitivity. The choice of mixing time is further influenced by the background decay.

Application of shaped observer pulses resulted in shorter echoes with higher peak intensity. However, evaluation of echo-integrated DEER and RIDME data revealed increased noise levels. The reason remains to be fully understood and calls for a dedicated study.

Orientation selection in DEER and RIDME was compared for Q-band traces with monochromatic observer pulses and a shaped pump pulse for DEER. In both cases, the dipolar spectrum changes with the observer position and for DEER it also changes with the position of the pump band relative to the observer band. Field-averaged data resulted in the same dipolar spectrum for RIDME and DEER measurements. The agreement between the dipolar spectra obtained by two methods that differ fundamentally in the selection of the pumped spins indicates that orientation selection is largely suppressed in the field-averaged data.

Based on our findings, the development of experiments using a relaxation block or shaped pulses is certainly promising large sensitivity gains for excitation of broad spectra – not only for high-spin centers [85,83] – but also for spin 1/2 systems, such as Cu(II) studied here. Using spin 1/2 systems alleviates problems occurring in high-spin systems, as for example distortions of distance distributions by level mixing [119] or harmonic overtones of the dipolar frequency [80,99]. Broadband excitation of spins that are not directly observed in echoes from shaped pulses, e.g. the pumped spins in the DEER experiment, certainly proved beneficial. Sweeping also the observer pulses appears to yield lower sensitivity, or even deteriorates sensitivity, yet promises other improvements, e.g. for orientation averaging. For example, an experiment in which the whole X-band Cu(II) spectrum is observed using a single frequency band with shaped observer pulses could be imagined. Currently it appears that shaped observer pulses may be more promising for experiments designed for Fourier Transform Evaluation than for experiments based on evaluation by echo integration. In this regard, we hope to inspire dedicated studies of echo intensities and noise levels in traces from shaped observer pulses.

Acknowledgments

The authors would like to thank Irina Ritsch and Yevhen Polyhach for fruitful discussions. This work was supported by the Swiss National Science Foundation (grant 200020_169057) and by the Deutsche Forschungsgemeinschaft (DFG) within SPP 1601 (GO555/6-2).

Appendix A. Supplementary material

Supplementary data associated with this article can be found, in the online version, at https://doi.org/10.1016/j.jmr.2019.07.047.

References

[1] W. Kaim, B. Schwederski, A. Klein, Bioinorganic Chemistry-Inorganic Elements in the Chemistry of Life: An Introduction and Guide, John Wiley & Sons, 2013.
[2] T.R. Hvidsten, A. Lægreid, A. Kryshtafovych, G. Andersson, K. Fidelis, J. Komorowski, A comprehensive analysis of the structure-function relationship in proteins based on local structure similarity, PloS One 4 (2009), e6266.
[3] C.R. Timmel, J.R. Harmer, Structural Information from Spin-Labels and Intrinsic Paramagnetic Centres in the Biosciences, volume 152, Springer, 2014.
[4] P. Borbat, A. Costa-Filho, K. Earle, J. Moscicki, J. Freed, Electron spin resonance in studies of membranes and proteins, Science 291 (2001) 266–269.
[5] M. Smyth, J. Martin, X-ray crystallography, Mol. Pathol. 53 (2000) 8.
[6] A. Lapinaite, B. Simon, L. Skjaerven, M. Rakwalska-Bange, F. Gabel, T. Carlomagno, The structure of the box c/d enzyme reveals regulation of RNA methylation, Nature 502 (2013) 519.
[7] H.J. de Groot, Solid-state NMR spectroscopy applied to membrane proteins, Curr. Opin. Struct. Biol. 10 (2000) 593–600.
[8] B.C. Bohrer, S.I. Merenbloom, S.L. Koeniger, A.E. Hilderbrand, D.E. Clemmer, Biomolecule analysis by ion mobility spectrometry, Annu. Rev. Anal. Chem. 1 (2008) 293–327.
[9] F. Lanucara, S.W. Holman, C.J. Gray, C.E. Eyers, The power of ion mobility-mass spectrometry for structural characterization and the study of conformational dynamics, Nat. Chem. 6 (2014) 281.
[10] L. Sleno, D.A. Volmer, Ion activation methods for tandem mass spectrometry, J. Mass Spectrom. 39 (2004) 1091–1112.
[11] D. Suckau, Y. Shi, S.C. Beu, M.W. Senko, J.P. Quinn, F. Wampler, F.W. McLafferty, Coexisting stable conformations of gaseous protein ions, PNAS 90 (1993) 790–793.
[12] E. Boeri Erba, C. Petosa, The emerging role of native mass spectrometry in characterizing the structure and dynamics of macromolecular complexes, Protein Sci. 24 (2015) 1176–1192.
[13] E. Haas, The study of protein folding and dynamics by determination of intramolecular distance distributions and their fluctuations using ensemble and single-molecule FRET measurements, ChemPhysChem 6 (2005) 858–870.
[14] B. Schuler, W.A. Eaton, Protein folding studied by single-molecule FRET, Curr. Opin. Struct. Biol. 18 (2008) 16–26.
[15] J. Lepault, F. Booy, J. Dubochet, Electron microscopy of frozen biological suspensions, J. Microsc. 129 (1983) 89–102.
[16] R. Fernandez-Leiro, S.H. Scheres, Unravelling biological macromolecules with cryo-electron microscopy, Nature 537 (2016) 339.
[17] T. Prisner, M. Rohrer, F. MacMillan, Pulsed EPR spectroscopy: biological applications, Annu. Rev. Phys. Chem. 52 (2001) 279–313.
[18] O. Schiemann, T.F. Prisner, Long-range distance determinations in biomacromolecules by EPR spectroscopy, Quart. Rev. Biophys. 40 (2007) 1–53.
[19] G. Jeschke, DEER distance measurements on proteins, Annu. Rev. Phys. Chem. 63 (2012) 419–446.
[20] T. Schmidt, M.A. Wälti, J.L. Baber, E.J. Hustedt, G.M. Clore, Long distance measurements up to 160 Å in the GroEL tetradecamer using Q-band DEER EPR spectroscopy, Angew. Chem. Int. Edit. 55 (2016) 15905–15909.
[21] G. Jeschke, The contribution of modern EPR to structural biology, Emerg. Top. Life Sci. 2 (2018) 9–18.
[22] R. Sundaramoorthy, A.L. Hughes, V. Singh, N. Wiechens, D.P. Ryan, H. El-Mkami, M. Petoukhov, D.I. Svergun, B. Treutlein, S. Quack, et al., Structural reorganization of the chromatin remodeling enzyme Chd1 upon engagement with nucleosomes, Elife 6 (2017), e22510.
[23] O. Duss, E. Michel, M. Yulikov, M. Schubert, G. Jeschke, F.H.-T. Allain, Structural basis of the non-coding RNA RsmZ acting as a protein sponge, Nature 509 (2014) 588–592.
[24] E. Bordignon, Site-directed spin labeling of membrane proteins, Top. Curr. Chem. 321 (2012) 121–157.
[25] W.L. Hubbell, C.J. Lopez, C. Altenbach, Z. Yang, Technological advances in site-directed spin labeling of proteins, Curr. Opin. Struct. Biol. 23 (2013) 725–733.
[26] G.E. Fanucci, D.S. Cafiso, Recent advances and applications of site-directed spin labeling, Curr. Opin. Struct. Biol. 16 (2006) 644–653.
[27] J.P. Klare, H.-J. Steinhoff, Spin labeling EPR, Photosynth. Res. 102 (2009) 377–390.
[28] A. Abragam, B. Bleaney, Electron Paramagnetic Resonance of Transition Metal Ions, Clarendon, Oxford, 1970.
[29] R. Cammack, Electron paramagnetic resonance spectroscopy of metalloproteins, in: C. Jones, B. Mulloy, A.H. Thomas (Eds.), Spectroscopic Methods and Analyses: NMR, Mass Spectrometry, and Metalloprotein Techniques, Humana Press, Totowa, NJ, 1993, pp. 327–344.
[30] S. Van Doorslaer, D.M. Murphy, EPR spectroscopy in catalysis, in: M. Drescher, G. Jeschke (Eds.), EPR Spectroscopy: Applications in Chemistry and Biology, Springer, Berlin Heidelberg, 2012, pp. 1–39.
[31] L.C. Dickinson, M. Symons, Electron spin resonance of haemoglobin and myoglobin, Chem. Soc. Rev. 12 (1983) 387–414.
[32] M. Bennati, M. Hertel, J. Fritscher, T. Prisner, N. Weiden, R. Hofweber, M. Spoerner, G. Horn, H.-R. Kalbitzer, High-frequency 94 GHz ENDOR characterization of the metal binding site in wild-type ras·GDP and its oncogenic mutant G12V in frozen solution, Biochemistry 45 (2006) 42–50.
[33] T. Wiegand, D. Lacabanne, K. Keller, R. Cadalbert, L. Lecoq, M. Yulikov, L. Terradot, G. Jeschke, B.H. Meier, A. Böckmann, Solid-state NMR and EPR spectroscopy of Mn^{2+}-substituted ATP-fueled protein engines, Angew. Chem. Int. Ed. 56 (2017) 3369–3373.
[34] Hervé Daubric, Janis Kliava, Philippe Guionneau, Daniel Chasseau, Jean-Francois Létard, Olivier Kahn, Spin transition in [Fe(PM-BiA)$_2$ (NCS)$_2$] studied by the electron paramagnetic resonance of the Mn^{2+} ion, J. Phys. Condens. Matter 12 (2000) 5481.
[35] G. Otting, Protein NMR using paramagnetic ions, Ann. Rev. Biophys. 39 (2010) 387–405.
[36] T.F. Cunningham, M.D. Shannon, M.R. Putterman, R.J. Arachchige, I. Sengupta, M. Gao, C.P. Jaroniec, S. Saxena, Cysteine-specific Cu^{2+} chelating tags used as paramagnetic probes in double electron electron resonance, J. Phys. Chem. B 119 (2015) 2839–2843.
[37] T.F. Cunningham, M.R. Putterman, A. Desai, W.S. Horne, S. Saxena, The double-histidine Cu^{2+}-binding motif: a highly rigid, site-specific spin probe for electron spin resonance distance measurements, Angew. Chem. Int. Ed. 54 (2015) 6330–6334.
[38] S. Ghosh, M.J. Lawless, G.S. Rule, S. Saxena, The Cu^{2+}-nitrilotriacetic acid complex improves loading of α-helical double histidine site for precise distance measurements by pulsed ESR, J. Magn. Reson. 286 (2018) 163–171.
[39] M.J. Lawless, S. Ghosh, T.F. Cunningham, A. Shimshi, S. Saxena, On the use of the Cu^{2+} iminodiacetic acid complex for double histidine based distance measurements by pulsed ESR, Phys. Chem. Chem. Phys. 19 (2017) 20959–20967.
[40] G.E. Merz, P.P. Borbat, A.R. Muok, M. Srivastava, D.N. Bunck, J.H. Freed, B.R. Crane, Site-specific incorporation of a Cu^{2+} spin label into proteins for measuring distances by pulsed dipolar electron spin resonance spectroscopy, J. Phys. Chem. B 122 (2018) 9443–9451.
[41] M. Qi, A. Groß, G. Jeschke, A. Godt, M. Drescher, Gd(III)-PyMTA label is suitable for in-cell EPR, J. Am. Chem. Soc. 136 (2014) 15366–15378.
[42] A. Martorana, G. Bellapadrona, A. Feintuch, E. Di Gregorio, S. Aime, D. Goldfarb, Probing protein conformation in cells by EPR distance measurements using Gd^{3+} spin labeling, J. Am. Chem. Soc. 136 (2014) 13458–13465.

[43] Y. Yang, F. Yang, Y.-J. Gong, T. Bahrenberg, A. Feintuch, X.-C. Su, D. Goldfarb, High sensitivity in-cell EPR distance measurements on proteins using an optimized Gd(III) spin label, J. Phys. Chem. Lett. 9 (2018) 6119–6123.
[44] Y. Yang, F. Yang, X.-Y. Li, X.-C. Su, D. Goldfarb, In-cell epr distance measurements on ubiquitin labeled with a rigid PyMTA-Gd(III) tag, J. Phys. Chem. B. 123 (2019) 1050–1059.
[45] M. Azarkh, A. Bieber, M. Qi, J.W. Fischer, M. Yulikov, A. Godt, M. Drescher, Gd(III)–Gd(III) relaxation-induced dipolar modulation enhancement for in-cell electron paramagnetic resonance distance determination, J. Phys. Chem. Lett. 10 (2019) 1477–1481.
[46] I. Krstić, R. Hänsel, O. Romainczyk, J.W. Engels, V. Dötsch, T.F. Prisner, Long-range distance measurements on nucleic acids in cells by pulsed EPR spectroscopy, Angew. Chem. Int. Ed. 123 (2011) 5176–5180.
[47] R. Hänsel, L.M. Luh, I. Corbeski, L. Trantirek, V. Doetsch, In-cell NMR and EPR spectroscopy of biomacromolecules, Angew. Chem. Int. Edit. 53 (2014) 10300–10314.
[48] A.P. Jagtap, I. Krstic, N.C. Kunjir, R. Hänsel, T.F. Prisner, S.T. Sigurdsson, Sterically shielded spin labels for in-cell EPR spectroscopy: analysis of stability in reducing environment, Free Rad. Res. 49 (2015) 78–85.
[49] I. Kaminker, H. Yagi, T. Huber, A. Feintuch, G. Otting, D. Goldfarb, Spectroscopic selection of distance measurements in a protein dimer with mixed nitroxide and Gd^{3+} spin labels, Phys. Chem. Chem. Phys. 14 (2012) 4355–4358.
[50] P. Lueders, G. Jeschke, M. Yulikov, Double electron-electron resonance measured between Gd^{3+} ions and nitroxide radicals, J. Phys. Chem. Lett. 2 (2011) 604–609.
[51] M. Yulikov, Chapter 1 Spectroscopically orthogonal spin labels and distance measurements in biomolecules, Electron. Paramag. Reson. 24 (2015) 1–31.
[52] R.G. Larsen, D.J. Singel, Double electron–electron resonance spin–echo modulation: spectroscopic measurement of electron spin pair separations in orientationally disordered solids, J. Chem. Phys. 98 (1993) 5134–5146.
[53] A. Schweiger, G. Jeschke, Principles of Pulse Electron Paramagnetic Resonance, Oxford University Press, 2001.
[54] G. Jeschke, Distance measurements in the nanometer range by pulse EPR, ChemPhysChem 3 (2002) 927–932.
[55] G. Jeschke, Dipolar spectroscopy–double-resonance methods, eMagRes (2007) 1459–1476.
[56] G. Jeschke, M. Pannier, A. Godt, H. Spiess, Dipolar spectroscopy and spin alignment in electron paramagnetic resonance, Chem. Phys. Lett. 331 (2000) 243–252.
[57] P.P. Borbat, J.H. Freed, Multiple-quantum ESR and distance measurements, Chem. Phys. Lett. 313 (1999) 145–154.
[58] S. Saxena, J.H. Freed, Double quantum two-dimensional Fourier transform electron spin resonance: distance measurements, Chem. Phys. Lett. 251 (1996) 102–110.
[59] J.S. Becker, S. Saxena, Double quantum coherence electron spin resonance on coupled Cu(II)-Cu(II) electron spins, Chem. Phys. Lett. 414 (2005) 248–252.
[60] S. Ruthstein, M. Ji, P. Mehta, L. Jen-Jacobson, S. Saxena, Sensitive Cu^{2+}–Cu^{2+} distance measurements in a protein–DNA complex by double-quantum coherence ESR, J. Phys. Chem. B 117 (2013) 6227–6230.
[61] A. Milov, A. Ponomarev, Y. Tsvetkov, Electron-electron double resonance in electron spin echo: model biradical systems and the sensitized photolysis of decalin, Chem. Phys. Lett. 110 (1984) 67–72.
[62] M. Pannier, S. Veit, A. Godt, G. Jeschke, H. Spiess, Dead-time free measurement of dipole-dipole interactions between electron spins, J. Magn. Reson. 142 (2000) 331–340.
[63] S. Milikisyants, F. Scarpelli, M.G. Finiguerra, M. Ubbink, M. Huber, A pulsed EPR method to determine distances between paramagnetic centers with strong spectral anisotropy and radicals: the dead-time free RIDME sequence, J. Magn. Reson. 201 (2009) 48–56.
[64] J.E. Lovett, A.M. Bowen, C.R. Timmel, M.W. Jones, J.R. Dilworth, D. Caprotti, S. G. Bell, L.L. Wong, J. Harmer, Structural information from orientationally selective DEER spectroscopy, Phys. Chem. Chem. Phys. 11 (2009) 6840–6848.
[65] A. Gamble Jarvi, K. Ranguelova, S. Ghosh, R.T. Weber, S. Saxena, On the use of Q-band double electron-electron resonance to resolve the relative orientations of two double histidine-bound Cu^{2+} ions in a protein, J. Phys. Chem. B 122 (2018) 10669–10677.
[66] D.M. Engelhard, A. Meyer, A. Berndhäuser, O. Schiemann, G.H. Clever, Di-copper (II) DNA G-quadruplexes as EPR distance rulers, ChemComm (2018).
[67] E. Narr, A. Godt, G. Jeschke, Selective measurements of a nitroxide-nitroxide separation of 5 nm and a nitroxide-copper separation of 2.5 nm in a terpyridine-based copper(II) complex by pulse EPR spectroscopy, Angew. Chem. Int. Edit. 41 (2002) 3907–3910.
[68] Z. Yang, J. Becker, S. Saxena, On Cu(II)-Cu(II) distance measurements using pulsed electron electron double resonance, J. Magn. Reson. 188 (2007) 337–343.
[69] B.E. Bode, J. Plackmeyer, T.F. Prisner, O. Schiemann, PELDOR measurements on a nitroxide-labeled Cu(II) porphyrin: orientation selection, spin-density distribution, and conformational flexibility, J. Phys. Chem. A 112 (2008) 5064–5073.
[70] I.M.C. van Amsterdam, M. Ubbink, G.W. Canters, M. Huber, Measurement of a Cu-Cu distance of 26 Å by a pulsed EPR method, Angew. Chem. Int. Edit. 42 (2003) 62–64.
[71] Z. Yang, M. Ji, S. Saxena, Practical aspects of copper ion-based double electron electron resonance distance measurements, Appl. Magn. Reson. 39 (2010) 487–500.
[72] Z. Yang, D. Kise, S. Saxena, An approach towards the measurement of nanometer range distances based on Cu^{2+} ions and ESR, J. Phys. Chem. B 114 (2010) 6165–6174.
[73] A.M. Bowen, C.E. Tait, C.R. Timmel, J.R. Harmer, Orientation-Selective DEER Using Rigid Spin Labels, Cofactors, Metals, and Clusters, Springer Berlin Heidelberg, pp. 283–327.
[74] G. Jeschke, V. Chechik, P. Ionita, A. Godt, H. Zimmermann, J. Banham, C.R. Timmel, D. Hilger, H. Jung, DeerAnalysis2006—a comprehensive software package for analyzing pulsed ELDOR data, Appl. Magn. Reson. 30 (2006) 473–498. <http://www.epr.ethz.ch/software.html>.
[75] A. Meyer, D. Abdullin, G. Schnakenburg, O. Schiemann, Single and double nitroxide labeled bis(terpyridine)-copper(II): influence of orientation selectivity and multispin effects on PELDOR and RIDME, Phys. Chem. Chem. Phys. 18 (2016) 9262–9271.
[76] A. Giannoulis, M. Oranges, B.E. Bode, Monitoring complex formation by relaxation-induced pulse electron paramagnetic resonance distance measurements, ChemPhysChem 18 (2017) 2318–2321.
[77] A.V. Astashkin, Chapter ten – mapping the structure of metalloproteins with RIDME, in: Peter Z. Qin, Kurt Warncke (Eds.), Meth. Enzymol., vol. 56, Academic Press, 2015, pp. 251–284.
[78] D. Abdullin, N. Florin, G. Hagelueken, O. Schiemann, EPR-based approach for the localization of paramagnetic metal ions in biomolecules, Angew. Chem. Int. Edit. 127 (2015) 1847–1851.
[79] A. Giannoulis, C.L. Motion, M. Oranges, M. Bühl, G.M. Smith, B.E. Bode, Orientation selection in high-field RIDME and PELDOR experiments involving low-spin Co(II) ions, Phys. Chem. Chem. Phys. 20 (2018) 2151–2154.
[80] S. Razzaghi, M. Qi, A.I. Nalepa, A. Godt, G. Jeschke, A. Savitsky, M. Yulikov, RIDME spectroscopy with Gd(III) centers, J. Phys. Chem. Lett. 5 (2014) 3970–3975.
[81] K. Keller, V. Mertens, M. Qi, A. Nalepa, A. Godt, A. Savitsky, G. Jeschke, M. Yulikov, Computing distance distributions from dipolar evolution data with overtones: RIDME spectroscopy with Gd(III)-based spin labels, Phys. Chem. Chem. Phys. 19 (2017) 17856–17876.
[82] K. Keller, M. Qi, C. Gmeiner, I. Ritsch, A. Godt, G. Jeschke, A. Savitsky, M. Yulikov, Intermolecular background decay in RIDME experiments, Phys. Chem. Chem. Phys. (2019).
[83] P.E. Spindler, P. Schöps, A.M. Bowen, B. Endeward, T.F. Prisner, Shaped pulses in EPR, eMagres (2016) 1477–1492.
[84] P.E. Spindler, P. Schöps, W. Kallies, S.J. Glaser, T.F. Prisner, Perspectives of shaped pulses for EPR spectroscopy, J. Magn. Reson. 280 (2017) 30–45.
[85] A. Doll, G. Jeschke, Wideband frequency-swept excitation in pulsed EPR spectroscopy, J. Magn. Reson. 280 (2017) 46–62.
[86] P.E. Spindler, Y. Zhang, B. Endeward, N. Gershernzon, T.E. Skinner, S.J. Glaser, T.F. Prisner, Shaped optimal control pulses for increased excitation bandwidth in EPR, J. Magn. Reson. 218 (2012) 49–58.
[87] A. Doll, S. Pribitzer, R. Tschaggelar, G. Jeschke, Adiabatic and fast passage ultra-wideband inversion in pulsed EPR, J. Magn. Reson. 230 (2013) 27–39.
[88] I. Kaminker, R. Barnes, S. Han, Arbitrary waveform modulated pulse EPR at 200 GHz, J. Magn. Reson. 279 (2017) 81–90.
[89] A. Band, M.P. Donohue, B. Epel, S. Madhu, V.A. Szalai, Integration of a versatile bridge concept in a 34 GHz pulsed/CW EPR spectrometer, J. Magn. Reson. 288 (2018) 28–36.
[90] T. Kaufmann, T.J. Keller, J.M. Franck, R.P. Barnes, S.J. Glaser, J.M. Martinis, S. Han, DAC-board based X-band EPR spectrometer with arbitrary waveform control, J. Magn. Reson. 235 (2013) 95–108.
[91] A. Doll, G. Jeschke, Fourier-transform electron spin resonance with bandwidth-compensated chirp pulses, J. Magn. Reson. 246 (2014) 18–26.
[92] P. Neugebauer, D. Bloos, R. Marx, P. Lutz, M. Kern, D. Aguilà, J. Vaverka, O. Laguta, C. Dietrich, R. Clérac, et al., Ultra-broadband EPR spectroscopy in field and frequency domains, Phys. Chem. Chem. Phys. 20 (2018) 15528–15534.
[93] M. Teucher, E. Bordignon, Improved signal fidelity in 4-pulse DEER with Gaussian pulses, J. Magn. Reson. 296 (2018) 103–111.
[94] G. Jeschke, S. Pribitzer, A. Doll, Coherence transfer by passage pulses in electron paramagnetic resonance spectroscopy, J. Phys. Chem. B (2015), 150513145858008.
[95] M. Silver, R. Joseph, C.-N. Chen, V. Sank, D. Hoult, Selective population inversion in NMR, Nature 310 (1984) 681.
[96] P.E. Spindler, I. Waclawska, B. Endeward, J. Plackmeyer, C. Ziegler, T.F. Prisner, Carr-Purcell pulsed electron double resonance with shaped inversion pulses, J. Phys. Chem. Lett. 6 (2015) 4331–4335.
[97] A. Tannus, M. Garwood, Improved performance of frequency-swept pulses using offset-independent adiabaticity, J. Magn. Reson.-Ser. A 120 (1996) 133–137.
[98] F.D. Breitgoff, J. Soetbeer, A. Doll, G. Jeschke, Y.O. Polyhach, Artefact suppression in 5-pulse double electron electron resonance for distance distribution measurements, Phys. Chem. Chem. Phys. 19 (2017) 15766–15779.
[99] A. Doll, M. Qi, N. Wili, S. Pribitzer, A. Godt, G. Jeschke, Gd(III)-Gd(III) distance measurements with chirp pump pulses, J. Magn. Reson. 259 (2015) 153–162.
[100] T. Bahrenberg, Y. Rosenski, R. Carmieli, K. Zibzener, M. Qi, V. Frydman, A. Godt, D. Goldfarb, A. Feintuch, Improved sensitivity for W-band Gd(III)-Gd(III) and nitroxide-nitroxide DEER measurements with shaped pulses, J. Magn. Reson. 283 (2017) 1–13.
[101] A. Doll, M. Qi, S. Pribitzer, N. Wili, M. Yulikov, A. Godt, G. Jeschke, Sensitivity enhancement by population transfer in Gd(III) spin labels, Phys. Chem. Chem. Phys. 17 (2015) 7334–7344.

[102] I. Ritsch, H. Hintz, G. Jeschke, A. Godt, M. Yulikov, Improving the accuracy of Cu(II)-nitroxide RIDME in the presence of orientation correlation evaluated with water-soluble Cu(II)-nitroxide rulers, Phys. Chem. Chem. Phys. (2019).

[103] J.S. Hyde, J.W. Sidabras, R.R. Mett, Uniform field resonators for EPR spectroscopy: a review, Cell Biochem. Biophys. (2018) 1–12.

[104] J.W. Sidabras, T. Sarna, R.R. Mett, J.S. Hyde, Uniform field loop-gap resonator and rectangular TEU02 for aqueous sample EPR at 94 GHz, J. Magn. Reson. 282 (2017) 129–135.

[105] R. Tschaggelar, F.D. Breitgoff, O. Oberhänsli, M. Qi, A. Godt, G. Jeschke, High-bandwidth Q-band EPR resonators, Appl. Magn. Reson. 48 (2017) 1273–1300.

[106] V. Denysenkov, P. van Os, T.F. Prisner, Q-band loop-gap resonator for EPR applications with broadband-shaped pulses, Appl. Magn. Reson. 48 (2017) 1263–1272.

[107] M. Qi, M. Hülsmann, A. Godt, Spacers for geometrically well-defined water-soluble molecular rulers and their application, J. Org. Chem. 81 (2016) 2549–2571.

[108] M. Qi, M. Hülsmann, A. Godt, Synthesis and hydrolysis of 4-chloro-PyMTA and 4-iodo-PyMTA esters and their oxidative degradation with Cu(I/II) and oxygen, Synthesis 48 (2016) 3773–3784.

[109] A. Doll, G. Jeschke, EPR-correlated dipolar spectroscopy by Q-band chirp SIFTER, Phys. Chem. Chem. Phys. 18 (2016) 23111–23120.

[110] R. Tschaggelar, B. Kasumaj, M.G. Santangelo, J. Forrer, P. Leger, H. Dube, F. Diederich, J. Harmer, R. Schuhmann, I. García-Rubio, G. Jeschke, Cryogenic 35 GHz pulse ENDOR probehead accommodating large sample sizes: performance and applications, J. Magn. Reson. 200 (2009) 81–87.

[111] K. Keller, A. Doll, M. Qi, A. Godt, G. Jeschke, M. Yulikov, Averaging of nuclear modulation artefacts in RIDME experiments, J. Magn. Reson. 272 (2016) 108–113.

[112] C.E. Tait, S. Stoll, Coherent pump pulses in double electron electron resonance spectroscopy, Phys. Chem. Chem. Phys. 18 (2016) 18470–18485.

[113] H. El Mkami, D.G. Norman, Chapter five – EPR distance measurements in deuterated proteins, in: P.Z. Qin, K. Warncke (Eds.), Methods in Enzymology, vol. 564, Academic Press, 2015, pp. 125–152.

[114] K. Keller, M. Zalibera, M. Qi, V. Koch, J. Wegner, H. Hintz, A. Godt, G. Jeschke, A. Savitsky, M. Yulikov, EPR characterization of Mn(II) complexes for distance determination with pulsed dipolar spectroscopy, Phys. Chem. Chem. Phys. 18 (2016) 25120–25135.

[115] S. Pribitzer, T.F. Segawa, A. Doll, G. Jeschke, Transverse interference peaks in chirp FT-EPR correlated three-pulse ESEEM spectra, J. Magn. Reson. 272 (2016) 37–45.

[116] P. Schöps, P.E. Spindler, A. Marko, T.F. Prisner, Broadband spin echoes and broadband SIFTER in EPR, J. Magn. Reson. 250 (2015) 55–62.

[117] A. Tannús, M. Garwood, Adiabatic pulses, NMR Biomed.: Int. J. Devot. Dev. Appl. Magn. Reson. In Vivo 10 (1997) 423–434.

[118] A. Savitsky, A.A. Dubinskii, M. Flores, W. Lubitz, K. Mobius, Orientation-resolving pulsed electron dipolar high-field EPR spectroscopy on disordered solids: I. Structure of spin-correlated radical pairs in bacterial photosynthetic reaction centers, J. Phys. Chem. B 111 (2007) 6245–6262.

[119] A. Dalaloyan, M. Qi, S. Ruthstein, S. Vega, A. Godt, A. Feintuch, D. Goldfarb, EPR distance measurements – the range of accessible distances and the impact of zero field splitting, Phys. Chem. Chem. Phys. 17 (2015) 18464–18476.

[120] R.D. Shannon, Revised effective ionic radii and systematic studies of interatomic distances in halides and chalcogenides, Acta Cryst. A 32 (1976) 751–767.

[121] J. Wort, K. Ackermann, A. Giannoulis, A. Stewart, D. Norman, B.E. Bode, Sub-micromolar pulse dipolar EPR spectroscopy reveals increasing CuII-labelling of double-histidine motifs with lower temperature, Angew. Chem. (2019), https://doi.org/10.1002/ange.201904848.

[122] S. Pribitzer, M. Sajid, M. Hülsmann, A. Godt, G. Jeschke, Pulsed triple electron resonance (TRIER) for dipolar correlation spectroscopy, J. Magn. Reson. 282 (2017) 119–128.

[123] D. Abdullin, F. Duthie, A. Meyer, E.S. Muller, G. Hagelueken, O. Schiemann, Comparison of PELDOR and RIDME for distance measurements between nitroxides and low-spin Fe(III) ions, J. Phys. Chem. B 119 (2015) 13534–13542.

[124] M.-E. Boulon, A. Fernandez, E.M. Pineda, N.F. Chilton, G. Timco, A.J. Fielding, R. E. Winpenny, Measuring spin-spin interactions between heterospins in a hybrid [2] rotaxane, Angew. Chem. Int. Edit. 129 (2017) 3934–3937.

[125] R. Mett, J. Sidabras, J. Hyde, Uniform radio frequency fields in loop-gap resonators for EPR spectroscopy, Appl. Magn. Reson. 31 (2007) 573.